Vacuum Calculations in Azimuthally Symmetric Geometry*

M. S. Chance
Princeton University Plasma Physics Laboratory,
P.O. Box 451, Princeton, NJ 08543, USA

Abstract

A robustly accurate and effective method is presented to solve Laplace's equation in general azimuthally symmetric geometry for the magnetic scalar potential in the region surrounding a plasma discharge which may or may not contain external conducting shells. These shells can be topologically toroidal or spherical, and may have toroidal gaps in them. The solution is incorporated into the various MHD stability codes either through the volume integrated perturbed magnetic energy in the vacuum region or through the continuity requirements for the normal component of the perturbed magnetic field and the total perturbed pressure across the unperturbed plasma-vacuum boundary. The method is based upon using Green's second identity and the method of collocation. As useful byproducts, the eddy currents and the simulation of Mirnov loop measurements are calculated.

PACS: 52.35.Py, 52.55.Fa, 52.55.Hc, 52.35.Bj

I. Introduction

The solution of the perturbed magnetic field in the vacuum region external to the plasma in toroidally symmetric tokamak discharges is essential for determining the external boundary conditions for stability analyses. As opposed to the cylindrical problem where the solutions of the magnetic scalar potential is readily obtained in terms of Bessel functions, the tokamak problem is two-dimensional and more general methods must be developed to incorporate the large variety of plasma cross-sectional shapes which now exist or are envisioned. In addition, there is usually a closed or partially closed shell surrounding the plasma, linking it toroidally or wholly enclosing it spherically, and quite often these have non-trivial geometrical configuration. It is convenient if a robust and accurate calculation of these effects is available to insure that numerical uncertainties in the overall stability calculations is isolated elsewhere. A good amount of 'overkill' is therefore built into the calculations for such assurances in the numerical accuracy. The code, 'VACUUM', described in the present work has undergone a steady evolution over the past several years and has been incorporated into many of the important MHD stability codes used in the present state-of-the-art numerical analyses for simulating plasma discharges and designing new devices. These stability codes initially include the PEST[1,2] and the NOVA[3] system of codes, and the modularity and flexibility built into the VACUUM code enables easy subsequent interfacing to other stability codes such as GATO[4] and DCON[5] as well. The evolution includes the ability to calculate and display the eddy current pattern in the conducting shells due to plasma perturbations, as well as the facility to simulate the Mirnov loop measurements of the perturbed magnetic field in the vacuum region in tokamak discharges. An important feature is the capability to incorporate the effects of a toroidally symmetric gap in the

*Work supported by U.S. Department of Energy Contract No. DE-AC02-76-CHO-3073.

shell since most tokamak devices need to have such a gap for heating beam lines, diagnostics, etc. Another feature mentioned above, the treatment of topologically spherical shell enclosing the whole plasma discharge, was used for analyzing the SPHEROMAK device.[6]

Although the method of solution given here is applicable to general problems requiring the solution of Laplace's equation in geometries with azimuthal symmetry, the emphasis here is on the MHD δW problem as formulated by Bernstein, et al.[7] There one needs only the volume integrated perturbed magnetic energy in the vacuum region as driven by the normal component of the surface perturbation of the plasma. In addition, the external shells are assumed perfectly conducting, and the volume energy can be easily transformed to a surface integral on the plasma-vacuum interface. The solution is obtained through the use of Green's second identity in which one of the functions is the free space Green's function for Laplace's equation. An integral equation is obtained in which the boundary conditions are naturally incorporated. This method has been used in a straight two-dimensional model with arbitrary cross-section in an investigation of the stability of the kink mode.[8]

The fundamental numerical technique used is the method of 'collocation'.[9] This is very effective when used with the free space Green's function, giving well-conditioned matrices, and its accuracy, as opposed to Fourier methods e.g., is based primarily only on the number of grid points defining the surfaces and the weights used to evaluate the quadratures. Because of the singular nature of the free space Green's function, great care must be taken when performing the integrals in the neighborhood of the singularities. These are dealt with accurately and appropriately so as to preserve the grid integrity of the collocation method. This method can incorporate the full grid information in the matrix manipulations, but Fourier, or finite element decomposition can be introduced when necessary for reducing *cpu* storage, or when it is used in the inhomogeneous source terms (i.e., the plasma-vacuum boundary conditions) as dictated by the specific application; in the latter case the basic accuracy of the method is not affected since the method of solution is independent of the sources. A comparison of a more primitive form of the present method and other methods have been presented elsewhere.[10] It is in contrast to the method used originally in the PEST code.[1] There, Green's second identity is also used but the Fourier decomposition is carried out before the quadratures, and thus inaccuracies involving the early truncation of the Fourier series are introduced. Another method using the Green's function technique is the original method used for the ERATO code,[11] in which the magnetic scalar potential is expanded in discrete finite elements in the plasma surface. This method has been replaced with one in which an equivalent magnetic vector potential instead is solved throughout the vacuum region.[12] Although this obviates some of the problems associated with singular kernels this can be inconvenient if the wall is far away or is made up of discrete conductors. The vector potential can be easily obtained from the scalar potential calculated in VACUUM and there is an option in the code which takes the vacuum energy from the Fourier basis to the finite element basis.

This paper discusses perturbations for which the toroidal mode number, n, is non-zero. The modification of the scalar potential method for axisymmetric modes as described by Lüst and Martensen[13] is positive definite so that the present rendition of the present code can still give a sufficient condition for stability for these modes.

II. Basic considerations

In rationalized Gaussian units with the speed of light, c = 1, the MHD system of equations relevant to this work are:[7]

$$\mathbf{J} \times \mathbf{B} = \nabla P, \tag{1}$$

with

$$\mathbf{J} = \nabla \times \mathbf{B}, \tag{2}$$

and

$$\mathbf{Q} = \nabla \times (\boldsymbol{\xi} \times \mathbf{B}). \tag{3}$$

In the vacuum region

$$\mathbf{Q}_v = \nabla \times \mathbf{A} = \nabla \chi, \tag{4}$$

where

$$\nabla \times \nabla \times \mathbf{A} = 0, \tag{5}$$

and

$$\nabla^2 \chi = 0. \tag{6}$$

Here, the equilibrium current, magnetic field and pressure are denoted respectively by $\mathbf{J}$, $\mathbf{B}$ and P, the perturbed magnetic field by $\mathbf{Q}$, and the plasma Lagrangian displacement by $\boldsymbol{\xi}$. $\mathbf{A}$ and χ are the magnetic vector and scalar potentials in the vacuum region. It is shown in the Appendix how one can determine these potentials from each other. The scalar potential will be calculated in terms of the radial component of the plasma displacement, $\xi_\psi (\equiv \boldsymbol{\xi} \cdot \nabla \psi)$, i.e., formally,

$$\chi = \mathsf{C}[\xi_\psi]. \tag{7}$$

As will be seen later, only the condition that the normal component of the perturbed magnetic field is continuous across the unperturbed plasma vacuum interface is used in deriving Eq. (7). The radial coordinate ψ, is taken to be proportional to the poloidal flux, $2\pi\psi$, and the equilibrium magnetic field can be represented as

$$\mathbf{B} = \nabla \phi \times \nabla \psi + g(\psi) \nabla \phi, \tag{8}$$

ϕ being the toroidal angle.

The effect of the perturbed magnetic field in the exterior region of the plasma discharge can be incorporated into the solution for the MHD equations for a tokamak by treating the problem as either a second order differential equation in the radial coordinate with appropriate boundary conditions on the dependent variables at the vacuum interface,[3] or as an integral variational problem where the vacuum effects enter as integral relations. The dependent MHD variables can be written in terms of ξ_ψ, together with its radial derivative, $\xi'_\psi (\equiv \partial \xi_\psi / \partial \psi)$, or the total plasma perturbed pressure, $p \equiv \delta p + \mathbf{B} \cdot \mathbf{Q}$. Since there is no fluid pressure in the vacuum, the total perturbed pressure there is given by:

$$p_v = \mathbf{B}_v \cdot \mathbf{Q}_v = \mathbf{B}_v \cdot \nabla \chi \tag{9}$$

$$= \mathbf{B}_v \cdot \nabla (\mathsf{C}[\xi_\psi]), \tag{10}$$

using Eq. (7), so that p_v is also cast in terms of the plasma displacement at the boundary. In the plasma, ξ'_ψ can be written in terms of p and ξ_ψ.[3] Using the pressure balance constraint at the boundary, $p = p_v$, and Eq. (10), a relation for ξ'_ψ/ξ at the boundary is obtained, and provides the boundary conditions required by the second order differential equation method.

In the case of the integral method, the *extended* energy principle[7,14] identifies the relevant integrals as contributions to the energy in the system and gives the widely used prescription for incorporating the surface and vacuum contributions into the total perturbed energy. In the extended form, the plasma perturbation satisfy the continuity of the normal component of the magnetic field, but, conveniently, need not satisfy pressure balance across the plasma-vacuum interface. The present work calculates both these relations, *cf.* Eqs. (7) and (10), so that the results are applicable to both the differential and integral methods.

For a Lagrangian plasma displacement, $\boldsymbol{\xi}$, the surface term is given by,

$$\delta W_s = \frac{1}{2}\int d\sigma(\mathbf{n}\cdot\boldsymbol{\xi})^2\mathbf{n}\cdot\left\langle\nabla\left(P+\frac{B^2}{2}\right)\right\rangle, \tag{11}$$

where $\langle X\rangle$ denotes the discontinuity of X across the boundary in the direction $\mathbf{n}(=\nabla\psi/|\nabla\psi|)$. If there is no skin current on the surface of the plasma, this term vanishes. To see this, note that if $\mathbf{b} = \mathbf{B}/B$, the curvature, $\boldsymbol{\kappa}$, of the magnetic field can be written as

$$\boldsymbol{\kappa} = \mathbf{b}\cdot\nabla\mathbf{b} \tag{12}$$

$$= \frac{1}{B^4}\mathbf{B}\times\left[\nabla\left(P+\frac{B^2}{2}\right)\times\mathbf{B}\right]. \tag{13}$$

Then

$$\mathbf{n}\cdot\nabla\left(P+\frac{B^2}{2}\right) = B^2\mathbf{n}\cdot\boldsymbol{\kappa}. \tag{14}$$

Since the magnetic field together with its curvature is continuous if there is no skin current at the plasma-vacuum interface, it follows that the surface contribution given by Eq. (11) vanishes.

The volume term can be expressed in terms of the vector or scalar potential for the magnetic field:

$$\delta W_v = \frac{1}{2}\int d\hat{\tau}|\nabla\times\mathbf{A}|^2 = \frac{1}{2}\int d\hat{\tau}|\nabla\chi|^2. \tag{15}$$

The calculation of this last quantity is the main focus of this work.

III. The solution for χ on the surfaces

The scalar potential is solved directly from an inhomogeneous Fredholm equation of the second kind with a non-symmetric singular kernel. Since the present numerical technique was intended for the PEST system of codes the emphasis here is to obtain a Fourier representation of the vacuum δW matrix. However, one can equally as well choose alternative representations, such as for example, the finite element decomposition used in the ERATO or GATO system of codes. In the section describing the Fourier analysis, Sec. IX, one should be able to replace the harmonic functions with other choices of expansion functions and recast the $\delta W_{\rm v}$ in the corresponding space. The analysis should be quite analogous. However, difficulties can be encountered because of the singular nature of the kernels. Alternatively, one can obtain the transformation which takes the vacuum matrix between the different representations. This is done in Sec. X

Green's second identity for the Laplacian with the observer points in the vacuum region and the source points on the plasma and conductor surfaces surrounding it gives†

$$4\pi\bar{\chi}(\mathbf{r}) + \int_S \bar{\chi}(\mathbf{r}')\nabla' G(\mathbf{r},\mathbf{r}')\cdot d\mathbf{S}' \quad = \quad \int_{S_p} G(\mathbf{r},\mathbf{r}')\nabla'\bar{\chi}(\mathbf{r}')\cdot d\mathbf{S}', \tag{16}$$

where $\bar{\chi}$, the magnetic scalar potential satisfies $\nabla^2\bar{\chi} = 0$ in the vacuum region. $G(\mathbf{r},\mathbf{r}')$ is chosen to be the free space Green's function for the Laplacian, i.e., $\nabla^2 G(\mathbf{r},\mathbf{r}') = -4\pi\delta(\mathbf{r}-\mathbf{r}')$. P denotes the principal value of the integral, and barred quantities here denote that the quantities contain their ϕ dependence. The boundary conditions are that the normal component of $\nabla\chi$ is continuous across the plasma vacuum-interface but vanishes on a conducting surface so that the second integral involves only the plasma surface S_p, and $S = S_p \cup S_c$. If there are no conductors then $S = S_p$, and the choice of the free space Green's function satisfies the appropriate boundary conditions at infinity. Writing $\bar{\chi}(\mathbf{r}) = \chi(\boldsymbol{\rho})\exp(-in\phi)$ because of toroidal symmetry, and suppressing the implicit n dependence of χ_n, one has

$$\begin{aligned}2\chi(\boldsymbol{\rho}) + \frac{1}{2\pi}\int_S e^{in(\phi-\phi')}\chi(\boldsymbol{\rho}')\nabla' G(\mathbf{r},\mathbf{r}')\cdot d\mathbf{S}' = \\ \frac{1}{2\pi}\int_{S_p} e^{in(\phi-\phi')}G(\mathbf{r},\mathbf{r}')\nabla'\chi(\boldsymbol{\rho}')\cdot d\mathbf{S}'.\end{aligned} \tag{17}$$

Because of the boundary conditions, the right hand side of Eq. (17) is treated as a known quantity so that one can solve for χ on S in terms of the plasma displacement on S_p. Using $d\mathbf{S}' = \mathcal{J}\nabla'\mathcal{Z}\; d\theta' d\phi'$, where $\nabla'\mathcal{Z}$ is normal to the vacuum surface in a coordinate system with $\mathcal{J} = (\nabla\mathcal{Z}\times\nabla\theta\cdot\nabla\phi)^{-1}$, one can write

$$2\chi(\boldsymbol{\rho}) + \int_C \chi(\theta')\mathcal{K}(\boldsymbol{\rho},\theta')\, d\theta' \quad = \quad \int_{C_p} \mathcal{G}(\boldsymbol{\rho},\theta')\mathcal{B}(\theta')\, d\theta', \tag{18}$$

where C is now the contour bounding the surface S in the (X,Z) plane. The function $\mathcal{G}$ is now a two-dimensional Green's function:

$$\mathcal{G}(\boldsymbol{\rho},\theta') \quad \equiv \quad \frac{1}{2\pi}\oint G(\mathbf{r},\mathbf{r}')e^{in(\phi-\phi')}\, d\phi', \tag{19}$$

$$\mathcal{K}(\boldsymbol{\rho},\theta') \quad \equiv \quad \frac{1}{2\pi}\oint \mathcal{J}\nabla' G(\mathbf{r},\mathbf{r}')\cdot\nabla'\mathcal{Z}e^{in(\phi-\phi')}\, d\phi', \tag{20}$$

and the source term is written as

$$\mathcal{B}(\theta') \quad = \quad \mathcal{J}\nabla'\chi\cdot\nabla'\mathcal{Z}. \tag{21}$$

In the ensuing calculations, the Jacobian information enters only implicitly through the distribution of observer and source points on S, i.e., through the parameterization, $[X(\theta), Z(\theta)]$. Some relevant properties of $\mathcal{G}$ and $\mathcal{K}$ will be described below.

To proceed, we need first only to calculate the χ on the surfaces. Since the kernels in the integrals are singular one needs to be careful to take the appropriate analytic continuation of Eq. (18). Then,

†The coordinate system used here is such that $\mathbf{r} = (x,y,z) = (\mathcal{Z},\theta,\phi) = (\psi,\theta,\phi) = (X,\phi,Z) = (\boldsymbol{\rho},\phi)$. Here $\boldsymbol{\rho}$ is the position vector in the (X,Z) plane.

separately denoting the scalar potential on the plasma and conducting surfaces by χ_p and χ_c, we arrive at a set of coupled integral equations for the surface perturbations. For $\boldsymbol{\rho}$ on the plasma surface,

$$\begin{aligned}\chi_p(\theta_p) + P\oint_{C_p} \chi_p(\theta_p')\mathcal{K}(\theta_p,\theta_p')d\theta_p' + \oint_{C_c} \chi_c(\theta_c')\mathcal{K}(\theta_p,\theta_c')d\theta_c' \\ = \oint \mathcal{G}(\theta_p,\theta_p')\mathcal{B}(\theta_p')d\theta_p'.\end{aligned} \tag{22}$$

Similarly, for $\boldsymbol{\rho}$ on the conducting surfaces,

$$\begin{aligned}\chi_c(\theta_c) + P\oint_{C_c} \chi_c(\theta_c')\mathcal{K}(\theta_c,\theta_c')d\theta_c' + \oint_{C_p} \chi_p(\theta_p')\mathcal{K}(\theta_c,\theta_p')d\theta_p' \\ = \oint \mathcal{G}(\theta_c,\theta_p')\mathcal{B}(\theta_p')d\theta_p'.\end{aligned} \tag{23}$$

In both of the preceding equations, the residue from the analytic continuation has cancelled one factor of χ_p and χ_c respectively, from the left hand sides. In the event that the conducting shells are far away only Eq. (22) survives with $\chi_c \to 0$.

Eqs. (22) and (23) must be solved for χ_p and χ_c in terms of $\mathcal{B}$. Formally, one can write the solution as

$$\chi(\theta) = \oint \mathcal{C}(\theta,\theta')\mathcal{B}(\theta')\, d\theta', \tag{24}$$

$\mathcal{C}$ being the response function of χ to the source $\mathcal{B}$.

IV. The response function for $\delta W_{\rm v}$

The energy contribution in the vacuum region is given by

$$\begin{aligned}2\delta W_{\rm v} &= \int_v |\nabla\bar{\chi}(\mathcal{Z},\theta',\phi')|^2\, dV && (25)\\ &= \int_v \nabla\cdot(\bar{\chi}^*\nabla\bar{\chi})\, dV && (26)\\ &= \int_{S_p} \bar{\chi}_p^*\nabla\bar{\chi}_p\cdot d\mathbf{S}, && (27)\end{aligned}$$

using the relation, $\nabla^2\bar{\chi} = 0$, and Gauss's theorem. This can be further expressed as

$$\begin{aligned}2\delta W_{\rm v} &= \int_{S_p} \bar{\chi}_p^*\nabla\bar{\chi}_p\cdot\nabla\mathcal{Z}\,\mathcal{J}\, d\phi'\, d\theta' && (28)\\ &= \int_{S_p} \chi_p^*(\theta')\mathcal{B}(\theta')e^{-i(n-n')\phi'}\, d\phi'\, d\theta' && (29)\\ &= 2\pi\int_{C_p} \chi_p^*(\theta')\mathcal{B}(\theta')\, d\theta', && (30)\\ &= 2\pi\int_{C_p} d\theta'\int_{C_p} d\theta''\, \mathcal{C}(\theta',\theta'')\mathcal{B}^*(\theta')\mathcal{B}(\theta''), && (31)\end{aligned}$$

where we used Eqs. (21) and (24).

Although the formalism described so far is straightforward the actual numerical implementation is complicated by the singular nature of the kernels in the integrals. To efficiently perform the quadratures over these integrable kernels some relevant features of the Green's function must be understood. These are described in the next section.

V. The Green's function and its properties

The three dimensional free space Green's function is

$$G(\mathbf{r},\mathbf{r}) \;=\; \frac{1}{|\mathbf{r}-\mathbf{r}'|}. \tag{32}$$

Integration over the toroidal angle ϕ', gives the two dimensional Green's function in (X,Z):

$$\mathcal{G}^n(\theta,\theta') \;\equiv\; \frac{1}{2\pi}\oint G(\mathbf{r},\mathbf{r}')e^{in(\phi-\phi')}\,d\phi', \tag{33}$$

which can be written as:

$$2\pi\mathcal{G}^n(\theta,\theta') \;=\; \oint d\phi\frac{e^{-in\phi}}{\sqrt{\rho^2+4XX'\sin^2(\phi/2)}}, \tag{34}$$

$$= \frac{2}{\sqrt{XX'}}\int_0^{\pi/2} d\phi\frac{\cos 2n\phi}{\sqrt{h^2+\sin^2\phi}}, \tag{35}$$

$$= \frac{2\pi^{1/2}\Gamma(1/2-n)}{\mathcal{R}}P^n_{-1/2}(s), \tag{36}$$

where $P^n_{-1/2}$ is the associated Legendre function of the first kind and $h^2=\rho^2/4XX'$, $\rho^2=(X-X')^2+(Z-Z')^2$, and

$$\mathcal{R}^2 \;=\; \sqrt{\rho^2(\rho^2+4XX')}, \tag{37}$$

$$s \;=\; \frac{X^2+X'^2+(Z-Z')^2}{\mathcal{R}^2}. \tag{38}$$

Note that $\mathcal{G}^n$ is symmetric with respect to interchange of (X,Z) and (X',Z') so that Heisenberg matrices formed from $\mathcal{G}^n$ will also have this property.

The gradient of $\mathcal{G}^n$ is written as:

$$\nabla'\mathcal{G}^n \;=\; \hat{e}_X\frac{\partial\mathcal{G}^n}{\partial X'}+\hat{e}_Z\frac{\partial\mathcal{G}^n}{\partial Z'} \tag{39}$$

$$\begin{aligned} =\; & \frac{2\pi^{1/2}\Gamma(1/2-n)}{\mathcal{R}^5}\left[\frac{\hat{e}_X}{X'}\left\{2XX'(X^2-X'^2+\zeta^2)P^{n+1}_{-1/2}(s)\right.\right. \\ & + \left.\left\{n(X^2+X'^2+\zeta^2)(X^2-X'^2+\zeta^2)-X'^2(X'^2-X^2+\zeta^2)\right\}P^n_{-1/2}\right\} \\ & + \left.\hat{e}_Z\zeta\left\{4XX'P^{n+1}_{-1/2}(s)+(2n+1)(X^2+X'^2+\zeta^2)P^n_{-1/2}(s)\right\}\right], \end{aligned} \tag{40}$$

where $\zeta\equiv(Z-Z')$, and to calculate the derivatives of the Legendre functions, we have made use of the recurrence relation,

$$(s^2-1)\frac{dP^\mu_\nu}{ds}(s) \;=\; (s^2-1)^{1/2}P^{\mu+1}_\nu(s)+\mu sP^\mu_\nu(s), \tag{41}$$

with

$$(s^2-1) \quad = \quad \frac{4X^2X'^2}{\rho^2(\rho^2+4XX')} = \frac{(2XX')^2}{\mathcal{R}^4}. \tag{42}$$

The Legendre functions are generated from the upward recurrence relation,

$$P^{n+1}_{-1/2}(s) \quad = \quad -\frac{2ns}{(s^2-1)^{1/2}}P^n_{-1/2}(s) - (n-1/2)^2 P^{n-1}_{-1/2}(s), \quad n = 1, 2, \ldots \tag{43}$$

$$P^1_{-1/2}(s) \quad = \quad \frac{1/2}{(s^2-1)^{1/2}}\left\{P^0_{1/2}(s) - sP^0_{-1/2}(s)\right\}. \tag{44}$$

These are initiated by their relations to the complete elliptic integrals of the first and second kinds, K and E, respectively:

$$P^0_{-1/2}(s) \quad = \quad \frac{2}{\pi}m_1^{1/2}K(m_1), \quad m_1 = \frac{2}{s+1}, \tag{45}$$

and

$$P^0_{1/2}(s) \quad = \quad \frac{2}{\pi}m_1^{1/2}E(m_1), \quad m_1 = \left[s + (s^2-1)^{1/2}\right]^{-2}. \tag{46}$$

The relations used here can be derived from equations found in Erdélyi[15] and Abramowitz and Stegun.[16] The latter reference also contains polynomial approximations for the elliptic integrals which are accurate to $O(10^{-8})$. It should be noted that no truncation problems associated with using the upward recurrence relations have been encountered for the practical values of n used in the applications.

The radial gradient of $\mathcal{G}^n$ is needed to calculate $\mathcal{K}$ in Eq. (20):

$$\mathcal{J}\nabla'\mathcal{G}^n \cdot \nabla'\mathcal{Z} \quad = \quad -X'\left[Z'_\theta\frac{\partial\mathcal{G}^n}{\partial X'} - X'_\theta\frac{\partial\mathcal{G}^n}{\partial Z'}\right], \tag{47}$$

where we have used the relations,

$$\mathcal{Z}_X \quad = \quad -Z_\theta\frac{X}{\mathcal{J}}, \tag{48}$$

and

$$\mathcal{Z}_Z \quad = \quad X_\theta\frac{X}{\mathcal{J}}. \tag{49}$$

Here $X'_\theta = \partial X'/\partial\theta$, etc. We note that, unlike $\mathcal{G}^n$, the kernel in $\mathcal{K}$ is not symmetric with respect to (X,Z) and (X',Z').

V.A. Limiting values

It can be shown that

$$2\pi\mathcal{G}^n \quad \underset{\rho\to 0}{\longrightarrow} \quad -\frac{2}{X'}\log\rho. \tag{50}$$

To see this, one can write the two-dimensional Green's function as:

$$2\pi\mathcal{G} \quad = \quad \frac{1}{\rho}\oint_0^{2\pi} d\phi''\frac{\exp -in\phi''}{\sqrt{1+(4XX'/\rho^2)\sin^2\phi''/2}} \tag{51}$$

$$= \quad \frac{4}{\rho}\int_0^{\pi/2} d\phi'\frac{\cos 2n\phi'}{\sqrt{1+(4XX'/\rho^2)\sin^2\phi'}}, \tag{52}$$

where the explicit $\exp -in\phi$ behavior has been dropped.

The leading singular term can be extracted by writing the integral as:

$$2\pi\mathcal{G} = \frac{4}{\rho}\left[\int_0^{\pi/2} d\phi' \frac{\cos 2n\phi' - \cos\phi'}{\sqrt{1+(4XX'/\rho^2)\sin^2\phi'}} \right.$$

$$\left. + \quad \int_0^{\pi/2} d\phi' \frac{\cos\phi'}{\sqrt{1+(4XX'/\rho^2)\sin^2\phi'}}\right] \tag{53}$$

$$\equiv \quad 2\pi[\mathcal{G}_{\rm reg} + \mathcal{G}_{\rm sing}]. \tag{54}$$

$\mathcal{G}_{\rm reg}$ is now well behaved as $\rho \to 0$, and the singularity is contained in $\mathcal{G}_{\rm sing}$ which can be evaluated analytically. This gives:

$$2\pi\mathcal{G}_{\rm sing} \quad = \quad \frac{2}{\sqrt{XX'}}\left[-\log\rho + \log\left(2\sqrt{XX'} + \sqrt{\rho^2 + 4XX'}\right)\right]. \tag{55}$$

Thus,

$$2\pi\mathcal{G} \quad = \quad \xrightarrow[\rho\to 0]{} \quad -\frac{2}{\sqrt{XX'}}\log\rho. \tag{56}$$

And since

$$\rho^2 \quad = \quad (X-X')^2 + (Z-Z')^2 \tag{57}$$

$$\to \quad (X_\theta^2 + Z_\theta^2)(\theta-\theta')^2, \tag{58}$$

then,

$$2\pi\mathcal{G}(\theta,\theta') \quad \to \quad -\frac{1}{\sqrt{XX'}}\log(\theta-\theta')^2. \tag{59}$$

Another useful limiting relation arises from the behavior as the source point, (X', Z'), approaches the major axis:

$$\mathcal{G}^n \quad \xrightarrow[X'\to 0]{} \quad \frac{1}{\rho}\left\{\delta_{n,0} - \frac{XX'}{\rho^2}\left(\delta_{n,0} - \frac{\delta_{n,1}+\delta_{n,-1}}{2}\right) + \cdots\right\} \tag{60}$$

$$\frac{\partial\mathcal{G}^n}{\partial X'} \quad \xrightarrow[X'\to 0]{} \quad \frac{X}{\rho}\left\{\frac{\delta_{n,1}+\delta_{n,-1}}{2} - \frac{X'}{X}\delta_{n,0} + \cdots\right\}. \tag{61}$$

Thus,

$$\chi \quad \xrightarrow[X'\to 0]{} \quad 0, \quad \text{for} \quad n \neq 0, \tag{62}$$

and

$$\delta B_X \quad = \quad \frac{\partial\chi}{\partial X'} \tag{63}$$

is finite **only** for $n = \pm 1$.

(64)

This last property is an intrinsic property of vector fields. Any vector field which has finite contribution across the major axis must be a perturbation with $n = 1$ at the axis. In particular, the *tilt* and the *shift* mode perturbations[6] in spheromak type plasmas are perturbations allowed by $\mathcal{G}^n$, so the result of this work is naturally applicable to these configurations.

Because of the derivatives, the singularity in the radial gradient of the Green's function, as given by Eqs. (40) and (47), is stronger than logarithmic. However, if $\mathbf{r}$ approaches $\mathbf{r}'$ along a constant $\mathcal{Z}$ surface the singularity is at most only logarithmic. This can be seen by substituting Eq. (50) into Eq. (47) and using $X - X' \sim X'_\theta(\theta - \theta')$, etc. Then the coefficient multiplying $(\theta - \theta')^{-2}$ is seen to behave like $(\theta - \theta')(Z'_\theta X'_\theta - X'_\theta Z'_\theta)$ and hence eliminates this singular term.

VI. Solution by collocation

The solution of Eq. (18) for the response function $\mathcal{C}$ of the scalar potential, χ, can be found by a variety of ways, among which are the Fourier method of the PEST[1] code, and the finite elements method of the ERATO[17] code. In those Galerkin techniques, the perturbation is expanded in a finite set of functions and the coefficients are obtained from the ensuing matrix equivalent of Eq. (18). Usually, the number of expansion functions used is a fraction of the available grid points thus introducing further truncation errors in the inversion of the matrix. Here, it is found directly by discretizing the integrals on C in the space of the total available grid points. In this way one attains maximal accuracy in the inversion. From Eqs. (22) and (23), the collocation method formally gives,

$$\begin{bmatrix} \delta_{ji} + \mathcal{K}^n_{ji}(p,p') & \mathcal{K}^n_{ji}(p,c') \\ \mathcal{K}^n_{ji}(c,p') & \delta_{ji} + \mathcal{K}^n_{ji}(c,c') \end{bmatrix} \begin{bmatrix} \chi_{p_i} \\ \chi_{c_i} \end{bmatrix} = \begin{bmatrix} \mathcal{G}^n_{jk}(p,p') \\ \mathcal{G}^n_{jk}(c,p') \end{bmatrix} \mathcal{B}_k(\theta'_p) \tag{65}$$

where repeated indices are to be summed over. Here,

$$\mathcal{K}^n_{ji}(c,p') \equiv w_i \mathcal{K}^n(\theta_{c_j}, \theta'_{p_i}) \tag{66}$$

$$\text{and} \qquad \mathcal{G}^n_{jk}(c,p') \equiv w_k \mathcal{G}^n(\theta_{c_j}, \theta'_{p_k}) \tag{67}$$

$$\text{etc.,} \tag{68}$$

where w is a weight function chosen appropriately for the quadratures. Because of the extremely high accuracy offered by the Euler-Maclaurin effect,[18] trapezoidal weights are chosen if the integrands are periodic and the integration range spans the period. Otherwise, Simpson weights are used.

In actuality, this method of collocation cannot be directly applied because of the singular nature of the kernels. However, the technique described in the next section to integrate over the singularities ensure that the advantage of the collocative method is preserved.

VII. Treatment of the singular regions

The accurate evaluation of the integrals in the neighborhood of the singularity of the kernels, $\mathcal{G}^n(\theta,\theta')$ and $\mathcal{K}^n(\theta,\theta')$ in Eqs. (22) and (23), is effected by subtracting and adding the analytically known behavior of the kernels in the singular region. The singular region occupies the range, $[\theta_{j-I}, \theta_{j+I}]$ about the singular point θ_j. There it is convenient to perform a $2I+1$ order interpolation on the unknown function. This maintains global grid uniformity and allows for very high accuracy since the interpolating functions are known and the singular integrals can be evaluated analytically. The modified, well behaved integrals involving the known kernel and interpolating polynomials are evaluated using a high order (eighth order here) Gaussian quadrature to ensure more than enough accuracy for the majority of applications. Since no grid points of the quadrature lie at a singular point numerical difficulties there are avoided.

VII.A. The first type of singularity

We write

$$S_1(\theta_j) = \int_{\theta_{j-I}}^{\theta_{j+I}} \mathcal{G}^n(\theta_j,\theta')f(\theta')\,d\theta' \tag{69}$$

$$= \sum_{i=-I}^{I} f_{j+i}\int_{\theta_{j-I}}^{\theta_{j+I}} \mathcal{G}^n(\theta_j,\theta')\alpha_i(\theta')\,d\theta', \tag{70}$$

where the unknown function , $f(\theta') = \mathcal{J}\nabla'\mathcal{Z}\cdot\nabla'\chi(\theta')$, and $\alpha_i(\theta')$ is the set of interpolating functions spanning $[\theta_{j-I},\theta_{j+I}]$. Then let

$$2\pi\mathcal{G}^n(\theta_j,\theta') = \left[2\pi\mathcal{G}^n(\theta_j,\theta') + \frac{1}{X_j'}\log(\theta_j-\theta')^2\right] - \frac{1}{X_j'}\log(\theta_j-\theta')^2, \tag{71}$$

thus isolating the singular behavior so that the quantity in the square brackets is well behaved, and integrals of the form

$$S_{1_i}(\theta_j) \equiv \int_{\theta_{j-I}}^{\theta_{j+I}} \alpha_i(\theta')\log(\theta_j-\theta')^2\,d\theta' \tag{72}$$

are done analytically. If five-points Lagrange interpolating polynomials are used for α_i, i.e., $I=2$, then one finds

$$S_{1_i}(\theta_j) = \int_0^{2\Delta} A_i(\theta)\log\theta^2\,d\theta, \tag{73}$$

where $\Delta = \theta_k - \theta_{k-1}$, the grid size, and $A_i(\theta) \equiv [\alpha_i(\theta_j-\theta)+\alpha_i(\theta_j+\theta)]$. Defining $p \equiv \theta/\Delta$, the values for the integrals are,

$$\begin{array}{ccc} i & A_i & S_{1_i} \\ 0 & (p^2-1)(p^2-4)/2 & 16\Delta(\log 2\Delta - 68/15)/15 \\ 1 & -p^2(p^2-4)/3 & 128\Delta(\log 2\Delta - 8/15)/45 \\ 2 & p^2(p^2-1)/12 & 28\Delta(\log 2\Delta - 11/105)/45 \end{array} \tag{74}$$

The integral of the well-behaved contribution is carried out using, as mentioned above, eight point Gaussian quadratures on either side of the singularity. Note that, formally, one can now express the relation about the singular region as,

$$S_1(\theta_j) = \sum_{i=-I}^{I} f_{j+i}\mathcal{G}^n_{eff}(\theta_j,\theta'_{j+i}), \tag{75}$$

where the effective kernel is now well behaved and the collocative form of the right hand side of Eq. (65) is thus preserved.

	Enclosing shell		Open type shell	
	θ'_p	θ'_c	θ'_p	θ'_c
θ_p	1	-2	1	0
θ_c	0	-1	0	1

Table 1: Residues, $\mathcal{K}^0_{Res}$, of Eq. (77) for source contours with coordinate, θ', and observer coordinate, θ on the plasma and conducting shell.

VII.B. The second type of singularity

We have integrals of the type

$$I(\theta) \quad = \quad \oint \chi(\theta')\mathcal{K}^n(\theta,\theta')\, d\theta' \tag{76}$$

where the kernel $\mathcal{K}^n$ is singular. $\mathcal{K}^0$ has the same dominant singular behavior and we can exploit its properties to isolate and evaluate the integrals over the singularities. Thus, by integrating Laplace's equation for $G(\mathbf{r},\mathbf{r}')$ over the volume occupied by the vacuum region and using Gauss's theorem together with the definition of $\mathcal{K}$ given by Eq. (20) with $n = 0$, one can show that[17]

$$\oint \mathcal{K}^0(\theta,\theta')\, d\theta' \quad \equiv \quad \mathcal{K}^0_{Res} \tag{77}$$

where $\mathcal{K}^0_{Res}$ is given in Table 1. Both the case for toroidal shells enclosing the plasma, Fig. 1a,b, and for toroidal shells only partially enclosing the plasma, Fig. 1c,d, are shown. In the latter case the closed contour of integration is the circumference of the shell whose thickness must be greater than the distance between grids points describing the shell. If both source and observer points are on the same surface, i.e., along the diagonals of Table 1, then the principal part of the Eq. (77) is taken. When θ and θ' are on different surfaces their values are parameterized and indexed for the numerics such that the kernels are singular when $\theta_i = \theta'_j$ with $i = j$. This is most easily accomplished when the wall is of the type as shown in Fig. 1a.

Subtracting and adding the singular behavior at θ'_s yields, formally, for integrals on either the plasma or conductor surface,

$$I(\theta) \quad = \quad \oint \left[\chi(\theta')\mathcal{K}^n(\theta,\theta') - \chi(\theta'_s)\mathcal{K}^0(\theta,\theta')\right] d\theta' + \mathcal{K}^0_{Res}\chi(\theta'_s), \tag{78}$$

and the integrand is now well-behaved. The regular integral over the region outside the singular region is directly discretized with weights, w_i, as

$$I_r(\theta_j) \quad = \quad \sum_i{}' \, w_i \left[\mathcal{K}^n(\theta_j,\theta'_i) - \delta_{ji}\sum_k{}' \, \mathcal{K}^0(\theta_j,\theta'_k)\right]\chi(\theta'_i), \tag{79}$$

where the restricted sum is taken over the closed set of points excluding the singular region $[\theta_{j-I}, \theta_{j+I}]$. This last relation can be effectively written as

$$I_r(\theta_j) \quad = \quad \sum_i{}' \, \mathcal{K}^n_{\mathit{eff}}(\theta_j,\theta'_i)\chi(\theta'_i). \tag{80}$$

In the singular region, $\chi(\theta)$ is expanded into interpolating polynomials, $\alpha_i(\theta)$, about the singular point, $\theta'_s = \theta'_j$, then the integral there is evaluated as follows:

$$I_s(\theta_j) \quad = \quad \sum_{i=-I}^{I} \chi(\theta'_{j+i}) \int_{\theta_{j-I}}^{\theta_{j+I}} \mathcal{K}^n(\theta_j,\theta')\alpha_i(\theta')\, d\theta' - \chi(\theta'_j)\int_{\theta_{j-I}}^{\theta_{j+I}} \mathcal{K}^0(\theta_j,\theta')\, d\theta' \tag{81}$$

$$= \sum_{i=-I}^{I} \chi(\theta'_{j+i}) \int_{\theta_{j-I}}^{\theta_{j+I}} \left\{ \mathcal{K}^n(\theta_j, \theta') \alpha_i(\theta') - \delta_{i,0} \mathcal{K}^0(\theta_j, \theta') \right\} d\theta', \tag{82}$$

and the integral, as for the first type, is evaluated to very high accuracy using eight-point Gaussian quadratures. The Lagrange polynomials used here satisfy $\alpha_i(\theta_j) = \delta_{ij}$ on the grid so that the integrands with $i \neq 0$ are finite.

Note that again, as for I_r, we can still express the the relation around singular region in terms of a well behaved kernel as,

$$I_s(\theta_j) = \sum_{i=-I}^{I} \mathcal{K}^n_{\mathit{eff}}(\theta_j, \theta'_{j+i}) \chi(\theta'_{j+i}), \tag{83}$$

so that for the whole range we have essentially the relation,

$$I(\theta_j) = \sum_i \mathcal{K}_{\mathit{eff}}(\theta_j, \theta'_i) \chi(\theta'_i) + \mathcal{K}^0_{Res}. \tag{84}$$

VIII. The coefficient matrix

When the singularities are treated as described in the previous section and the residues explicitly included, the matrix equation, Eq. (65), is recast in terms of effective, well-behaved kernels, $\mathcal{K}_{ji}$ and $\mathcal{G}_{ji}$, as follows,

$$\begin{bmatrix} 2\delta_{ji} + \mathcal{K}_{ji}(p, p') & -2\delta_{ji} + \mathcal{K}_{ji}(p, c') \\ \mathcal{K}_{ji}(c, p') & \mathcal{K}_{ji}(c, c') \end{bmatrix} \begin{bmatrix} \chi_{p_i} \\ \chi_{c_i} \end{bmatrix} = \begin{bmatrix} \mathcal{G}_{jk}(p, p') \\ \mathcal{G}_{jk}(c, p') \end{bmatrix} \mathcal{B}_k(\theta'_p) \tag{85}$$

If the conducting shell does not enclose the plasma then the sense of the integrals around the shell is different and Eq. (85) is modified in accordance with Table 1. Thus:

$$\begin{bmatrix} 2\delta_{ji} + \mathcal{K}_{ji}(p, p') & \mathcal{K}_{ji}(p, c') \\ \mathcal{K}_{ji}(c, p') & 2\delta_{ji} + \mathcal{K}_{ji}(c, c') \end{bmatrix} \begin{bmatrix} \chi_{p_i} \\ \chi_{c_i} \end{bmatrix} = \begin{bmatrix} \mathcal{G}_{jk}(p, p') \\ \mathcal{G}_{jk}(c, p') \end{bmatrix} \mathcal{B}_i k\theta'_p) \tag{86}$$

The latter form is used if there is a poloidal gap in the shell as shown in Fig. 1c,d. For the case of no conductors only the upper left block in Eqs. (85) and (86) survives, and if there are more than one discrete conductor external to the plasma, these formulas are easily generalized. Formally then, we can write the discretized form of Eqs. (22) and (23) as,

$$\sum_i A_{ji} \chi(\theta_i) = \oint_{C_p} \mathcal{G}(\theta_j, \theta') \mathcal{B}(\theta')\, d\theta', \tag{87}$$

which can be solved directly for χ:

$$\chi(\theta_i) = \sum_j A^{-1}_{ji} \oint_{C_p} \mathcal{G}(\theta_j, \theta') \mathcal{B}(\theta')\, d\theta', \tag{88}$$

so that

$$\mathcal{C}(\theta_i, \theta') = \sum_j A^{-1}_{ji} \mathcal{G}(\theta_j, \theta'), \tag{89}$$

where A_{ji} is given by Eq. (85) or (86). The summation is taken over all the surfaces enclosing the vacuum, i.e., those of the plasma and all the conductors, if any.

We note here that the single matrix A_{ji} contains the contributions *in toto* from the plasma surface and all the conductors. This is in contrast to other methods[1,17] which separate out individual contributions of χ on the plasma and conductor surfaces, leaving a set of linear simultaneous equations to be solved. This method is useful if computational storage space is limited since the individual matrices are smaller. Unless one is careful however, the order in which the various χ contributions are eliminated can lead to singularities, especially when $n = 0$.

Substituting $\mathcal{C}$ from Eq. (89) into Eq. (31) and discretizing the integrals, one obtains

$$2\delta W_{\rm v} = \sum_{ik}^{p} \mathcal{R}_{ik} \mathcal{B}^*(\theta'_k)\mathcal{B}(\theta'_i), \tag{90}$$

where the index i corresponds to descretizing the integral in Eq. (30), and k to the one in Eq. (87), both over the plasma surface. The notation $\sum^p$ denotes that the summation involves only the points on the plasma surface. The response function, $\mathcal{R}$, to the plasma perturbation, $\mathcal{B}$, is thus found to be

$$\mathcal{R}_{ik} \equiv 2\pi\, w_i w_k \sum_j A_{ji}^{-1} \mathcal{G}(\theta_j, \theta'_k), \tag{91}$$

$$= 2\pi w_i w_k \mathcal{C}(\theta_i, \theta'_k). \tag{92}$$

As mentioned before, although $\mathcal{G}$ is symmetric with respect to its arguments, the matrix. A_{ji} is not symmetric. It turns out, however, that the final response function is in fact symmetric.

IX. Fourier analysis

For the PEST codes, the sources are Fourier analyzed in a coordinate system where the field lines are straight in the θ–ζ plane. Here θ is chosen to have some flexibility by specifying $\mathcal{J}$, and ζ is the resulting ignorable toroidal angle, which is expressed as

$$\zeta = \phi + \nu(\theta) \tag{93}$$

$$= \phi + q(\psi)\theta - \int_0^\theta \frac{\mathbf{B}\cdot\nabla\phi}{\mathbf{B}\cdot\nabla\theta}\, d\theta \equiv \phi + q(\psi)(\theta - \theta_p), \tag{94}$$

where the notation in the PEST code is such that $\nu(\psi,\theta) = -q(\psi)\delta(\psi,\theta)$. Here $q(\psi)$ is the safety factor and θ_p is the poloidal angle in the straight field line coordinates (θ_p, ϕ), so that $\delta(\psi,\theta)$ is the deviation of θ from this angle.

Linear perturbed quantities are assumed to have the behavior

$$\sim e^{i(l\theta - n\zeta)} = e^{i[l\theta - n\nu(\theta)] - in\phi} \tag{95}$$

and the ancillary θ dependence involved in $\nu(\theta)$ must be explicitly included in the Fourier decomposition of $\mathcal{B}$, i.e.,

$$\mathcal{B}(\theta') = \sum_l \mathcal{B}_l e^{i[l\theta' - n\nu(\theta')]}, \tag{96}$$

so that from Eq. (90)

$$2\delta W_{\rm v} = 2\pi \sum_{ll'} \mathcal{B}^*_{l'} \mathcal{B}_l \sum_{ik}^{p} w_i w_k \sum_j A_{ji}^{-1} \mathcal{G}(\theta_j, \theta'_k) e^{-i[l'\theta'_k - n\nu(\theta'_k)]} e^{i[l\theta'_i - n\nu(\theta'_i)]} \tag{97}$$

$$= \sum_{ll'} \mathcal{R}_{ll'} \mathcal{B}^*_{l'} \mathcal{B}_l, \tag{98}$$

where, in Fourier space, the response function has the form,

$$\mathcal{R}_{ll'} = 2\pi \sum_{ik}^{p} w_i w_k \sum_j A^{-1}_{ji} \mathcal{G}(\theta_j, \theta'_k) e^{-i[l'\theta'_k - n\nu(\theta'_k)]} e^{i[l\theta'_i - n\nu(\theta'_i)]}, \tag{99}$$

or

$$= 2\pi \sum_{ik}^{p} w_i w_k \mathcal{C}(\theta_i, \theta'_k) e^{-i[l'\theta'_k - n\nu(\theta'_k)]} e^{i[l\theta'_i - n\nu(\theta'_i)]}. \tag{100}$$

In practice, to save on computational storage space, the sum over the index k is carried out early in the calculation. This corresponds to integrating Eq. (87) with the explicit θ dependence of $\mathcal{B}$ given by the complex conjugate of Eq. (96). This does not affect the basic accuracy of the method since the source term is considered here as the external driver for the problem. One can then write

$$\mathcal{R}_{ll'} = 2\pi \sum_{i}^{p} \sum_j w_i A^{-1}_{ji} \mathcal{G}^*_{l'}(\theta_j) e^{i[l\theta'_i - n\nu(\theta'_i)]}, \tag{101}$$

where

$$\mathcal{G}^*_{l'}(\theta_j) \equiv \oint_{C_p} \mathcal{G}(\theta_j, \theta'_k) e^{-i[l'\theta'_k - n\nu(\theta'_k)]}\, d\theta'_k \tag{102}$$

$$= \sum_{k}^{p} w_k \mathcal{G}(\theta_j, \theta'_k) e^{-i[l'\theta'_k - n\nu(\theta'_k)]} \tag{103}$$

$$= \mathcal{G}^{*R}_{l'}(\theta_j) + i\mathcal{G}^{*I}_{l'}(\theta_j), \tag{104}$$

where

$$\mathcal{G}^R_{l'}(\theta_j) = \oint_{C_p} \mathcal{G}(\theta_j, \theta'_k) \cos[l'\theta'_k - n\nu(\theta'_k)]\, d\theta'_k, \tag{105}$$

and

$$\mathcal{G}^I_{l'}(\theta_j) = \oint_{C_p} \mathcal{G}(\theta_j, \theta'_k) \sin[l'\theta'_k - n\nu(\theta'_k)]\, d\theta'_k. \tag{106}$$

Note that from Eq. (88) the response function of $\chi(\theta)$ can also be expressed as

$$\chi(\theta_i) = \sum_l \mathcal{C}_l(\theta_i) \mathcal{B}_l, \tag{107}$$

where

$$\mathcal{C}_l(\theta_i) = \sum_j A^{-1}_{ij} \mathcal{G}_l(\theta_j), \tag{108}$$

$$= \mathcal{C}^R_l(\theta_i) + i\mathcal{C}^I_l(\theta_i). \tag{109}$$

Separating real and imaginary parts, and substituting these expressions into Eq. (101) gives finally,

$$\mathcal{R}_{ll'} = [\mathcal{A}^{RR}_{ll'} + \mathcal{A}^{II}_{ll'}] + i[\mathcal{A}^{IR}_{ll'} - \mathcal{A}^{RI}_{ll'}], \tag{110}$$

where

$$\mathcal{A}^{RR}_{ll'} \equiv 2\pi \sum_{i}^{p} w_i \cos[l\theta'_i - n\nu(\theta'_i)] \mathcal{C}^R_{l'}(\theta_i) \tag{111}$$

$$\mathcal{A}^{II}_{ll'} \equiv 2\pi \sum_i^p w_i \sin[l\theta'_i - n\nu(\theta'_i)]\mathcal{C}^I_{l'}(\theta_i) \tag{112}$$

$$\mathcal{A}^{IR}_{ll'} \equiv 2\pi \sum_i^p w_i \sin[l\theta'_i - n\nu(\theta'_i)]\mathcal{C}^R_{l'}(\theta_i) \tag{113}$$

$$\mathcal{A}^{RI}_{ll'} \equiv 2\pi \sum_i^p w_i \cos[l\theta'_i - n\nu(\theta'_i)]\mathcal{C}^I_{l'}(\theta_i). \tag{114}$$

For vertically symmetric configurations, $\mathcal{A}^{IR}_{ll'}$ and $\mathcal{A}^{RI}_{ll'}$ vanishes. The explicit form of the source term given by Eq. (87) or (96) have been purposely treated as unknown up to this point since the analysis is valid for an arbitrary source. In the MHD stability problem this is given by the continuity of the normal magnetic field across the plasma-vacuum interface. Thus, if $\mathcal{Z}$ is chosen to be the poloidal flux function, ψ, as in the PEST codes, then

$$\bar{\mathcal{B}}(\theta') = \mathcal{J}\,\bar{\mathbf{Q}}\cdot\nabla\psi, \tag{115}$$

where $\bar{\mathbf{Q}}$ is the perturbed magnetic field in the plasma:

$$\bar{\mathbf{Q}} = \nabla\times(\bar{\boldsymbol{\xi}}\times\mathbf{B}), \tag{116}$$

and

$$\mathcal{J}\bar{\mathbf{Q}}\cdot\nabla\psi = \mathcal{J}\mathbf{B}\cdot\nabla\bar{\xi}_\psi \tag{117}$$

$$= i\sum_l (l-nq)\xi_l e^{i(l\theta-n\zeta)}, \tag{118}$$

where Eqs. (94) and (8) are used. Barred quantities again signify that they have their dependence on ϕ. Here, $\bar{\xi}_\psi \equiv \bar{\boldsymbol{\xi}}\cdot\nabla\psi$, is the normal component of the plasma displacement on the surface.

Thus, one has

$$\mathcal{B}_l = i(l-nq)\xi_l, \tag{119}$$

so that from Eq. (107),

$$\chi(\theta_i) = i\sum_l (l-nq)\mathcal{C}_l(\theta_i)\xi_l \tag{120}$$

and from Eq. (98),

$$2\delta W_{\mathrm{v}} = \sum_{ll'}(l-nq)(l'-nq)\mathcal{R}_{ll'}\xi^*_{l'}\xi_l. \tag{121}$$

The vacuum response matrix to the plasma perturbation, $\bar{\xi}_l$, is therefore given by

$$V_{ll'} = (l-nq)(l'-nq)\mathcal{R}_{ll'}. \tag{122}$$

X. Transformation between bases

The vacuum matrices in different bases bases can be transformed into each other by the appropriate orthogonal transformation which is described here.

Denoting the transpose of v by $\tilde{v}$, the sources can be expanded in both bases as follows:

$$\mathcal{B}(\theta) = \sum_k \tilde{\mathcal{B}}_k \tau_k(\theta) = \sum_l \tilde{\mathcal{B}}_l \varphi_l(\theta), \tag{123}$$

where both τ_k and φ_l are orthonormal basis elements satisfying

$$\frac{1}{2\pi}\oint \tilde{\tau}_k(\theta)\tau_{k'}(\theta)d\theta = \delta_{kk'} \tag{124}$$

$$\text{and} \qquad \frac{1}{2\pi}\oint \tilde{\varphi}_l(\theta)\varphi_{l'}(\theta)d\theta = \delta_{ll'}; \tag{125}$$

then Eq. (123) gives

$$\frac{1}{2\pi}\oint \tilde{\tau}_k(\theta)\mathcal{B}(\theta)d\theta = \mathcal{B}_k = \sum_l \mathcal{B}_l \oint \tilde{\tau}_k(\theta)\varphi_l(\theta)d\theta, \tag{126}$$

$$= \sum_l T_{kl}\mathcal{B}_l, \tag{127}$$

$$\text{where} \qquad T_{kl} = \frac{1}{2\pi}\oint \tilde{\tau}_k(\theta)\varphi_l(\theta)d\theta. \tag{128}$$

Similarly, one finds

$$\mathcal{B}_l = \sum_k T_{lk}\mathcal{B}_k, \tag{129}$$

$$\text{where} \qquad T_{lk} = \frac{1}{2\pi}\oint \tilde{\varphi}_l(\theta)\tau_k(\theta)d\theta. \tag{130}$$

The transformation of the vacuum matrix from φ basis to the τ basis is as follows:

$$2\delta W_{\mathrm{v}} = \sum_{ll'} \tilde{\mathcal{B}}_l^* V_{ll'}\mathcal{B}_{l'} \tag{131}$$

$$= \sum_{ll'}\sum_k \tilde{\mathcal{B}}_k^* \tilde{T}_{kl} V_{ll'} \sum_{k'} T_{l'k'}\mathcal{B}_{k'} \tag{132}$$

$$= \sum_{kk'} \tilde{\mathcal{B}}_k^* V_{kk'}\mathcal{B}_{k'}, \tag{133}$$

$$\text{where} \qquad V_{kk'} = \sum_{ll'} \tilde{T}_{kl}^* V_{ll'} T_{l'k'}. \tag{134}$$

Since

$$\mathcal{B}_k = \sum_l T_{kl}\mathcal{B}_l = \sum_l T_{kl}\sum_{k'} T_{lk'}\mathcal{B}_{k'} \tag{135}$$

$$= \sum_{k'} \mathcal{B}_{k'}\left(\sum_l T_{kl}T_{lk'}\right), \tag{136}$$

the transformation matrix T_{kl} satisfies the orthonormality condition,

$$\sum_l T_{kl}T_{lk'} = \delta_{kk'}, \tag{137}$$

and so T is orthogonal.

Specializing to the case where $\varphi_l = e^{il\theta}$, and τ_k is a (tophat) finite element, let $\tau_k(\theta)$ be piecewise constant spanning two or more grid points on θ:

$$\tau_k(\theta) = \begin{cases} N^{1/2}, & \text{if } \theta_k - \pi/N \le \theta \le \theta_k + \pi/N \\ 0, & \text{otherwise} \end{cases} \tag{138}$$

$$\text{where} \qquad \theta_k = (2k-1)\frac{\pi}{N}, \tag{139}$$

and N is the number of finite elements in the interval $[0, 2\pi]$. The normalization is chosen so that

$$\frac{1}{2\pi}\int_0^{2\pi} \tilde{\tau}_{k'}^*(\theta)\tau_k(\theta)d\theta \quad = \quad \delta_{kk'}, \tag{140}$$

in analogy to the Fourier orthonormality property. Then one obtains:

$$T_{lk} \quad = \quad \frac{1}{2\pi}\oint \tau_k(\theta)e^{-il\theta}d\theta \tag{141}$$

$$\quad = \quad \frac{1}{2\pi}\oint \tau_k(\theta)(\cos l\theta - i\sin l\theta)d\theta \tag{142}$$

$$\quad \equiv \quad T^C_{lk} - iT^S_{lk}. \tag{143}$$

Similarly,

$$T_{kl} \quad = \quad T^C_{kl} + iT^S_{kl}, \tag{144}$$

so that

$$\sum_l \left[T^C_{kl}T^C_{lk'} + T^S_{kl}T^S_{lk'}\right] + i\left[T^S_{kl}T^C_{lk'} - T^C_{kl}T^S_{lk'}\right] \quad = \quad \delta_{kk'}, \tag{145}$$

or

$$\Big[\mathsf{T}^C\tilde{\mathsf{T}}^C + \mathsf{T}^S\tilde{\mathsf{T}}^S\Big] + i\Big[\mathsf{T}^S\tilde{\mathsf{T}}^C - \mathsf{T}^C\tilde{\mathsf{T}}^S\Big] \quad = \quad \mathsf{I}. \tag{146}$$

Since τ_k is piecewise constant one can get analytic expressions for T_{kl}:

$$T^C_{kl} \quad = \quad \frac{N^{1/2}}{\pi l}\cos\frac{l\pi}{N}(2k-1)\sin\frac{l\pi}{N} \tag{147}$$

$$T^S_{kl} \quad = \quad \frac{N^{1/2}}{\pi l}\sin\frac{l\pi}{N}(2k-1)\sin\frac{l\pi}{N}, \tag{148}$$

or

$$T_{kl} \quad = \quad \frac{N^{1/2}}{\pi l}\sin\frac{l\pi}{N}\exp\left\{i\frac{l\pi}{N}(2k-1)\right\}, \tag{149}$$

and the orthonormality relation takes the form,

$$\sum_{l=-L}^{L}\frac{N}{\pi^2 l^2}\sin^2\frac{l\pi}{N}\exp\left\{i\frac{2l\pi}{N}(k-k')\right\} \quad = \quad \delta_{kk'}, \tag{150}$$

where the imaginary part vanishes because of the odd parity in l. In practice, this relation need not be satisfied precisely to obtain very high accuracy in the calculation of $V_{kk'}$ in Eq. (134).

The complementary relation is

$$\sum_{k=1}^{N}\frac{N}{\pi^2 ll'}\sin\frac{l\pi}{N}\sin\frac{l'\pi}{N}\exp\left\{i\frac{\pi}{N}(2k-1)(l-l')\right\} \quad = \quad \delta_{ll'}, \tag{151}$$

and performing the sum over k in this case gives

$$\frac{N}{\pi^2 ll'}\sin\frac{l\pi}{N}\sin\frac{l'\pi}{N}\frac{\sin\pi(l-l')}{\sin\{\pi(l-l')/N\}}\exp\{i\pi(l-l')\} \quad = \quad \delta_{ll'}. \tag{152}$$

The imaginary part clearly vanishes for integer $l-l'$. For $l = l'$, the real part satisfies:

$$\frac{N^2}{\pi^2 l^2}\sin^2\frac{l\pi}{N} \quad \to \quad 1, \tag{153}$$

as $N/l \to \infty$.

XI. Conducting shell options

There are several options for the shape of the conducting shell in the vacuum region surrounding the plasma. These different topologies are illustrated in Fig. 1.

These range from a simple circular or D-shaped configuration Fig. 1a, to more complex shapes which need not fully enclose the plasma but can be arbitrarily shaped solid entities themselves in the vacuum region, Fig. 1c), d). A shell which has a toroidal gap as demanded by the accessibility in a tokamak device for beam lines, diagnostics etc., falls in the latter category. Similarly, the spheromak[6] device demands that the shell is topologically spherical, fully enclosing but not linking the toroidal plasma, Fig. 1b. This feature of the present work depends on the properties of the Green's function discussed in Sec. V.A and has been used to study the stability properties of the *tilting* and *shifting* modes in the spheromak device.[6] While the shapes can be numerically given, especially if the shape originates from an actual device, the configurations are more conveniently given analytically. Then we are assured that at least the first few derivatives are 'smooth' enough for numerical accuracy, especially if one needs to do interpolations during the numerical procedures. The following subsections describes some available options for the shape of the conductors. Some care must be taken when parameterizing the shell that it doesn't intersect the plasma. Some definitions used here are the plasma 'radius', $p_{\rm rad}$ and the plasma center (X_{cen}, X_{cen}), which are defined by:

$$p_{\rm rad} \equiv \frac{1}{2}(X_{max} - X_{min}), \tag{154}$$

$$X_{cen} = \frac{1}{2}(X_{max} + X_{min}), \tag{155}$$

and

$$Z_{cen} = \frac{1}{2}(Z_{min} + Z_{max}), \tag{156}$$

where X_{min} and X_{max} are respectively, the minimum and the maximum x-values of the plasma, etc.

XI.A. Simple toroidal *D*-shaped shell

This configuration where the shell is centered at c_w, has an elongation factor of b_w, a triangularity skewness d_w, and a radius in the equatorial plane of a, is given by the relation,

$$X_{w_i} = c_w + a\cos(\theta_i + d_w \sin\theta_i), \tag{157}$$

$$Z_{w_i} = -\, b_w a \sin\theta_i. \tag{158}$$

This gives a free-standing shell independent of the plasma position or dimensions, and is useful if the shell is from the simulation of an actual device. A convenient parameterization which is scaled to the plasma is given by,

$$X_{w_i} = X_{cen} + p_{\rm rad} c_w + p_{\rm rad}(1 + a - c_w)\cos(\theta_i + d_w \sin\theta_i), \tag{159}$$

$$Z_{w_i} = -\, b_w p_{\rm rad}(1 + a - c_w)\sin\theta_i. \tag{160}$$

Here the center of the shell is offset by $p_{\rm rad}c_w$ in the equatorial plane and is still a distance $p_{\rm rad}a$ from the outer major radius side of the plasma.

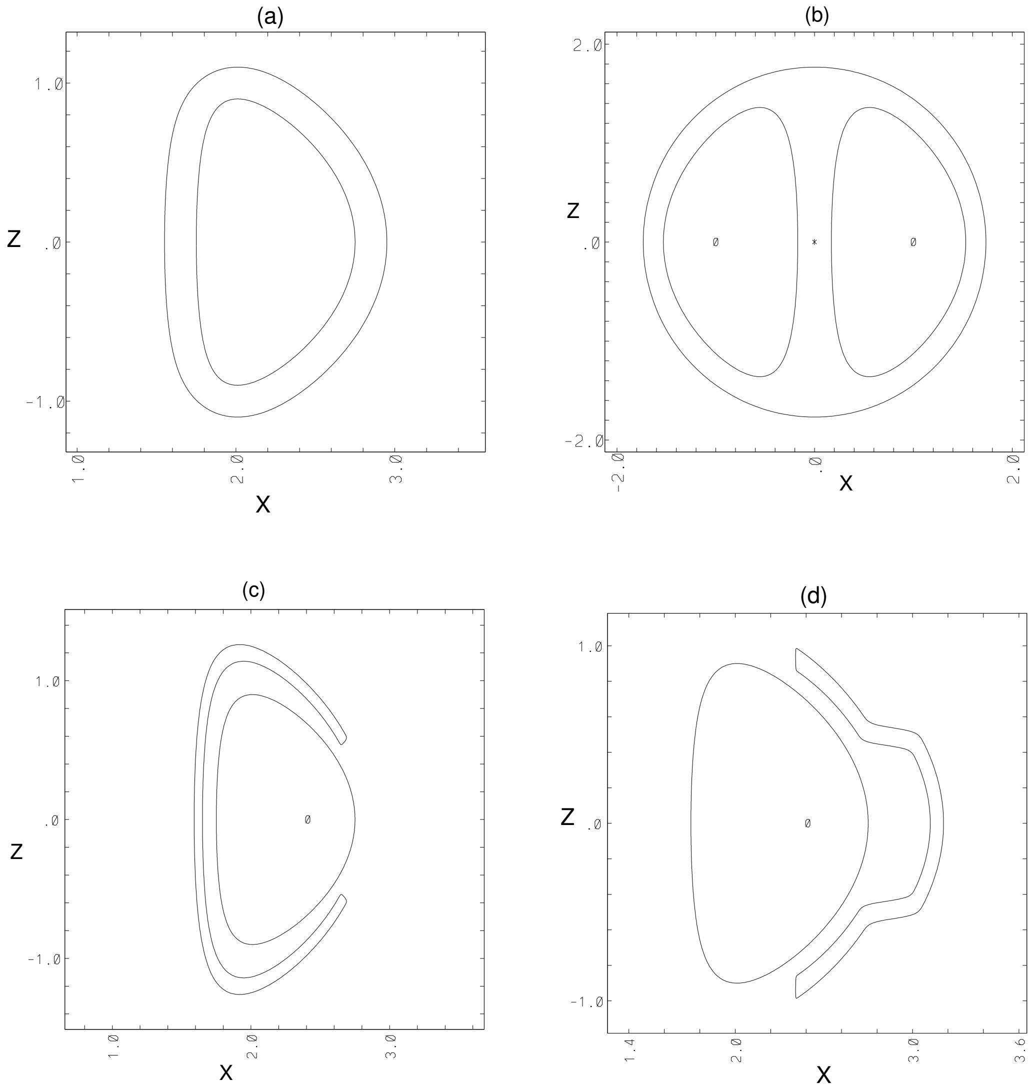

Figure 1: The three types of external conductors which are treated. a) Toroidal shell totally enclosing the plasma, and here placed equidistantly at $0.4p_{\rm rad}$ from the plasma. The D–shaped plasma surface parameters are $X_{cen} = 2.25$, $p_{\rm rad} = 0.5$, elongation = 1.8 and triangularity = 0.5. b) A spherical shell which doesn't link the plasma. c), d) Toroidal shells only partially enclosing the plasma.

XI.B. Toroidal equidistant shell

The equidistant option places the shell at a constant normal distance, $p_{\rm rad}a$ from the plasma. This option, illustrated in Fig. 1a, with $a = 0.4$ is a subset of the aforementioned D-shaped shell and is used quite frequently for scoping studies. It is convenient for simple repeatable quantizations of wall effects on MHD instabilities. It is also the easiest to place very close to the plasma surface because of the manner in which the plasma-wall grid points are aligned. These are calculated to first order in the grid size by placing each wall node at a distance $p_{\rm rad}a$ from the corresponding plasma node along the perpendicular from the line joining the two adjacent plasma nodes. Thus,

$$X_{w_i} = X_{p_i} + p_{\rm rad} a \cos \alpha_i \tag{161}$$

$$Z_{w_i} = Z_{w_i} + p_{\rm rad} a \sin \alpha_i \tag{162}$$

where

$$\alpha_i = \arctan \left(X_{w_{i+1}} - X_{w_{i-1}}, Z_{w_{i-1}} - Z_{w_{i+1}} \right) \tag{163}$$

The 'arctan' function here is used in the sense of *Fortran* function, $atan2$. This conveniently gives the correct branch of α_i throughout the entire perimeter of the plasma cross section. Note that the plasma and shell points are aligned in indices. As inferred form Sec. VII, this alignment is essential in the treatment of the singularities when the wall is placed close to the plasma. Care must be taken when using this option for plasmas with indented cross sections like that of the PBX device, since the wall could fold back into itself in the indented region.

XI.C. The segmented conducting shell

The class of segmented conducting shells which can be treated so far is basically variations on a finite-thickness dee-shaped wall at some variable distance from the plasma. As shown in Fig. 1c), d), there is only one up-down and toroidally symmetric gap in the shell. More gaps can be added with a moderate of work, but with a judicious choice of parameters we have found that, for the applications made so far, for example in PBX,[19,20] HBT-EP,[21] and TPX,[22] this is sufficient to effectively evaluate the effects which gaps may have in a surrounding conducting shell. Even within this restriction there are several options:

- The wall can be positioned and scaled with respect to the plasma dimensions or can be parameterized independent of the plasma.
- The wall can have the variably sized gap on the outer, Fig. 1c, or inner, Fig. 1d, major radius side of the torus.
- If the gap is on the inner major radius side, the wall may be further deformed to have a variably sized bulge at the outer major radius side Fig. 1d. This is useful when the upper and lower arms need to be electrically connected but the induced currents in the connections do not provide any direct stabilization.
- The segmented wall must have a thickness (cf. Fig. 1c,d)) because of mathematical and numerical difficulties associated with grid points across the thickness of the plates being too close to each other. This thickness can be varied. This is of course the more realistic situation if finite resistivity is included in the calculations.

- The sharpness of the corners of the plate defining the wall can be varied.
- The triangularity and elongation is specified as is usual in a closed wall.

XI.C.1. Wall referenced to the plasma size and position

The parameterization of the wall with a toroidally symmetric cut-out on the $^{\text{left}}_{\text{right}}$, with $0 \le \theta_0 \le 2\pi$, is given in the VACUUM code by

$$X_w(\theta_0) \;=\; X_{cen} + c_w p_{\rm rad} \pm \rho\cos(\theta_2 \pm \delta_w \sin\theta_2) + \mathcal{B}(a_b, \beta_b, \tau_b) \tag{164}$$

$$Z_w(\theta_0) \;=\; -\, b_w \rho \sin\theta_2, \tag{165}$$

where ρ contains a Fermi-like function to define the double-sided wall. The sharpness of the corners of the edges of the wall is determined by the 'temperature', τ_w, of the Fermi distribution:

$$\rho \;=\; a_0 \mp p_{\rm rad} a_w \left[1 - \frac{2}{e^{\cos\theta/\tau_w} + 1} \right]. \tag{166}$$

Note that as $\tau_w \to 0$ the quantity in the square brackets approaches ± 1 as $\cos\theta \to \pm$.

The bulge at the outer radius of the segmented wall is contained in the quantity $\mathcal{B}(a_b, \beta_b, \tau_b)$, also defined with a Fermi-like distribution:

$$\mathcal{B}(a_b, \beta_b, \tau_b) \;=\; p_{rad} a_b \left[\frac{1}{e^{(\cos 2\beta_b - \cos 2\theta_2)/\tau_b} + 1} \right], \tag{167}$$

τ_b, in this case being a measure of the inverse roundedness of the bulge, a_b the extent of the bulge along the major radius, and β_b the subtending half-angle of the outer side of the bulge. The inner side of bulge subtends an angle which is smaller by the quantity, $\delta\beta_b$, given by

$$\delta\beta_b \;=\; \frac{2a_w}{b_w(1 + a - c_w + 2a_w)} \frac{1 - \sin\beta_b}{\cos\beta_b}, \tag{168}$$

this so that the wall thickness, $2a_w$, remains approximately uniform throughout the bulge.

In these expressions we have

$$\theta_2 \;=\; \frac{\pi\beta}{180} \sin\theta, \tag{169}$$

$$\theta \;=\; \theta_0 - \frac{a_w p_{\rm rad}}{a_0} \sin 2\theta_0, \tag{170}$$

and

$$a_0 \;=\; p_{\rm rad}(1 + a_w - c_w + a). \tag{171}$$

Here, note that a_w, c_w, and a are in units of the plasma 'radius', $p_{\rm rad}$ defined above. The wall distance, a, is measured along the equatorial plane from the outer edge of the plasma to the inner edge of the conductor. a_0, δ_w and b_w are the radius, triangularity and elongation of the shape of the wall. a_w and τ_w are its half-width, and degree of sharpness of its ends, respectively. The inner/outer radii are thus $a_0 \mp a_w p_{\rm rad}$. Its center is displaced by c_w from X_{cen}, and β is the half-angle which it subtends. The concepts of 'center' and 'radius' of the shell here is referenced to the equatorial plane. The transformation given in Eq. (170) makes the distribution of the grid points defining the shell more uniform, especially at its corners. The parameters of Fig. 1d are $a = 0.20$, $\beta = 65.0°$, $a_w = 0.075$, $b_w = 1.90$, $c_w = 0.20$, $\delta_w = 0.50$, $\tau_w = 0.025$, $a_b = 0.50$, $\beta_b = 47.0°$ and $\tau_b = 0.02$.

XI.C.2. Wall independent of plasma

This is useful for the case when the wall for a real device is already in place like PBX and the wall is fixed but the plasma shape and position can be varied. The parameterization is similar to the above but all references to the plasma are taken out:

$$X_w(\theta_0) = c_w \pm \rho \cos(\theta_2 \pm \delta_w \sin \theta_2) \tag{172}$$

$$Z_w(\theta_0) = - b_w \rho \sin \theta_2, \tag{173}$$

where

$$\rho = a_0 \mp a_w \left[1 - \frac{2}{1 + e^{\cos \theta / \tau_w}} \right] \tag{174}$$

$$\theta = \theta_0 - \frac{a_w}{a_0} \sin 2\theta_0, \tag{175}$$

$$a_0 = a + a_w, \tag{176}$$

and the rest of the definitions are as described in the previous section. The lengths now are absolute, ie., not scaled to the plasma. The shell is now centered at c_w and its inner 'radius' is a where, as above, the center and the radius are referenced to the equatorial plane. The parameters making the shape in Fig. 1c are $a = 0.570$, $\beta = 152.3°$, $a_w = 0.030$, $b_w = 2.0$, $c_w = 2.22$, $\delta_w = 0.50$ and $\tau_w = 0.02$.

XI.D. Topologically spherical shells

This configuration is an azimuthally symmetric, ellipsoidal shell whose grid points are constructed along rays originating from the geometric center of the plasma at (X_{cen}, Z_{cen}) and emanating through the corresponding plasma grid points to provide alignment for treating the singular integrals if the shell approaches too close to the plasma. The shape is parameterized relative to the plasma shape by the pair of values, a_w and b_w, such that the horizontal and vertical axes in the X–Z plane are given respectively by $h_{rad} = X_{max} + a_w p_{\mathrm{rad}}$, and $v_{rad} = Z_{max} + b_w(Z_{max} - Z_{cen})$. Then the shell coordinates are given by

$$X_{w_i} = X_{cen} + H_i, \tag{177}$$

$$Z_{w_i} = Z_{cen} + t_i H_i. \tag{178}$$

Here

$$H_i = \frac{b}{G_i} \left[-X_{cen} v_{rad} + h_{rad} \left(G_i - t_i^2 X_{cen}^2 \right)^{1/2} \right], \tag{179}$$

where $G_i = v_{rad}^2 + t_i^2 h_{rad}^2$, and $t_i = (Z_{p_i} - Z_{cen})/(X_{p_i} - X_{cen})$. Accommodations must be made for using only those points projected for positive X. Such a shell is shown in Fig. 1b with $a_w = 0.3$, $b_w = 0.3$. Shell configurations of this type were used for stability studies of spheromak type plasmas.[6]

XII. Induced fields on the conducting shell

The eddy currents on the conducting shell induced by the plasma surface motion can be readily calculated from the magnetic scalar potential at the wall , χ_c, obtained in section III. This surface current is given by

$$\mathbf{K} = \hat{\mathbf{n}} \times \nabla \chi_c. \tag{180}$$

The X, Z, ϕ, and poloidal surface components are respectively,

$$K_X = -\frac{X_\theta}{X(X_\theta^2 + Z_\theta^2)^{1/2}} \frac{\partial \chi_c}{\partial \phi}, \tag{181}$$

$$K_Z = -\frac{Z_\theta}{X(X_\theta^2 + Z_\theta^2)^{1/2}} \frac{\partial \chi_c}{\partial \phi}, \tag{182}$$

$$K_\phi = \frac{1}{(X_\theta^2 + Z_\theta^2)^{1/2}} \frac{\partial \chi_c}{\partial \theta}, \tag{183}$$

$$K_\theta \equiv -\frac{\nabla\psi \times \nabla\phi}{|\nabla\psi||\nabla\phi|} \cdot \mathbf{K} = -\frac{1}{X} \frac{\partial \chi_c}{\partial \phi}. \tag{184}$$

Inserting the $\exp(-in\phi)$ dependence and using Eq. (120), the real parts of $\partial\chi_c/\partial\phi$ and $\partial\chi_c/\partial\theta$ can be written as:

$$\frac{\partial \chi_{c_r}}{\partial \phi} = n \sum_l \left[\mathcal{C}_l^R(\theta) \cos(n\phi) + \mathcal{C}_l^I(\theta) \sin(n\phi) \right] (l - nq) \xi_l \tag{185}$$

and

$$\frac{\partial \chi_{c_r}}{\partial \theta} = \sum_l \left[\frac{\partial \mathcal{C}_l^R(\theta)}{\partial \theta} \sin(n\phi) - \frac{\partial \mathcal{C}_l^I(\theta)}{\partial \theta} \cos(n\phi) \right] (l - nq) \xi_l. \tag{186}$$

The components in Cartesian coordinates, (x, y, z), useful for constructing projections of the current patterns are

$$K_x = K_X \cos\phi - K_\phi \sin\phi, \tag{187}$$

$$K_y = K_X \sin\phi + K_\phi \cos\phi, \tag{188}$$

$$K_z = K_Z. \tag{189}$$

The current distribution can also be displayed on an unfolded rectilinear ϕ–θ plane. To aid in the visualization the components of the current are scaled to $\widetilde{\mathbf{K}}$ as follows:

$$\widetilde{K}_\phi = \alpha L_\theta K_\phi, \tag{190}$$

$$\widetilde{K}_\theta = \alpha L_\phi(\theta) K_\theta, \tag{191}$$

where

$$\alpha \equiv \left(\frac{K_\phi^2 + K_\theta^2}{L_\theta^2 K_\phi^2 + L_\phi^2(\theta) K_\theta^2} \right)^{1/2}. \tag{192}$$

Here, $L_\phi(\theta) = 2\pi X(\theta)$, and L_θ is the minor circumference of the toroidal shell, or the distance between the $X = 0$ points along the longitude in the case of the spheroidal shell. This scaling tends to preserve the magnitude and direction of the current vectors when seen in the distorted ϕ–θ plane.

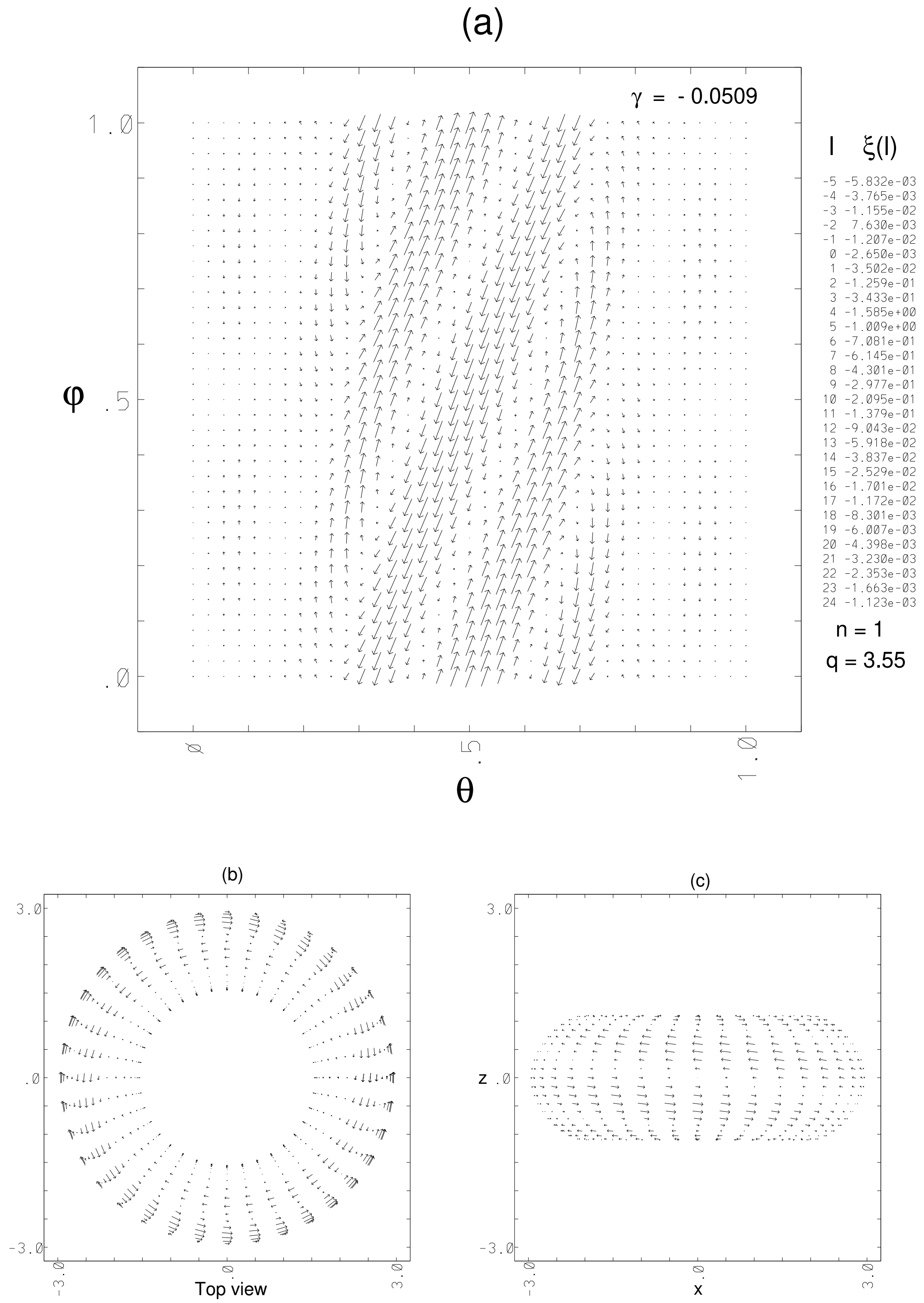

Figure 2: a) The eddy current pattern over one period in the ϕ–θ plane on the shell of Fig. 1a. Note the localization of the current on the outer major radius side of the shell. The side bar shows the Fourier components of the plasma surface perturbation, ξ_l. The projections of the current pattern as seen from above b) and the side c) of the shell are also shown

Knowledge of the magnitude and the distribution of **K** can be useful since the current pattern induced on the shell is generated by Lentz's law to suppress the growth of the plasma perturbation. Examination of the pattern enables economical use of the passive conducting material necessary for at least slowing down the dangerous external kink modes. This current pattern also provides valuable information for constructing a positive feedback system since such a system could ideally (but perhaps not practically) be effected by just enhancing the induced current pattern seen in the shell. Such studies were done for PBX. The calculation of these currents can also provide quantitative information about the stresses generated in the tokamak vacuum vessels due to perturbations, or more violent disruption-like processes. An example of such a current pattern on the shell of Fig. 1a enclosing an $n = 1$ kink unstable plasma is shown in Fig. 2. There the projection of the induced current is seen on the shell over one period in the unfolded ϕ–θ plane. Top and side views are also shown in the figure. Even though the shell is placed equidistantly from the plasma the current is localized in the vicinity of the outer major radius side of the plasma because of the 'bad curvature' effects on the kink mode there. The Fourier components, ξ_l, of the radial plasma displacement at the surface of the plasma is shown in side bar. This result emphasizes the importance for locating any stabilizing passive plates or active circuits on the outboard side of the plasma. This is usually in conflict with the requirements for access to the plasma for diagnostics, beam lines, waveguides, etc. so that a gap in the critical area such as shown in Fig. 1c is present. It's important to assess the decrease in the effectiveness of the shell due to this gap.[22,19] The dependency of the growth rates versus wall coverage using the gapped configuration is consistent with the induced current pattern shown here. These patterns are in good agreement with their experimentally observed counterparts in the HBT-EP device at Columbia University.[21]

The usefulness of the eddy current pattern is further illustrated by considering an idealized shifting or tilting mode[6] for a spheromak-like plasma with major radius 0.85, minor radius 0.68, elongation 2.0 and triangularity 0.45 with the topologically spherical conducting shell shown in Fig. 1b. A pure shifting or tilting mode will result if the plasma configuration is extremely oblate or prolate. A single shape is chosen for both for illustrative purposes. For the shifting mode, a surface perturbative displacement of the form $\xi_{-1} = +1$, and $\xi_{+1} = +1$ is imposed artificially, and the safety factor at the edge is set to zero. This perturbation corresponds to a rigid horizontal displacement of the plasma which induces a current pattern whose magnetic field and the plasma equilibrium current result in a restoring $\mathbf{J} \times \mathbf{B}$ force.[6] The induced current pattern is shown as a projection in the ϕ–θ plane in Fig. 3a, as viewed from the top b), and in two orthogonal views in the equatorial plane c), d). These considerations were significant factors which led to the design of appropriate stabilizing "figure-8" feedback coils against the shift mode in the S-1 spheromak device.[23] The corresponding induced current patterns for the pure tilt mode with $\xi_{-1} = +1$, and $\xi_{+1} = -1$ on the same plasma configuration is shown in Fig. 4.

One can also easily calculate the induced magnetic field on the shell. Because of the boundary conditions, the field at the shell lies within the plane of the shell. The components are given by:

$$Q_X = \frac{X_\theta}{X_\theta^2 + Z_\theta^2} \frac{\partial \chi_c}{\partial \theta},$$

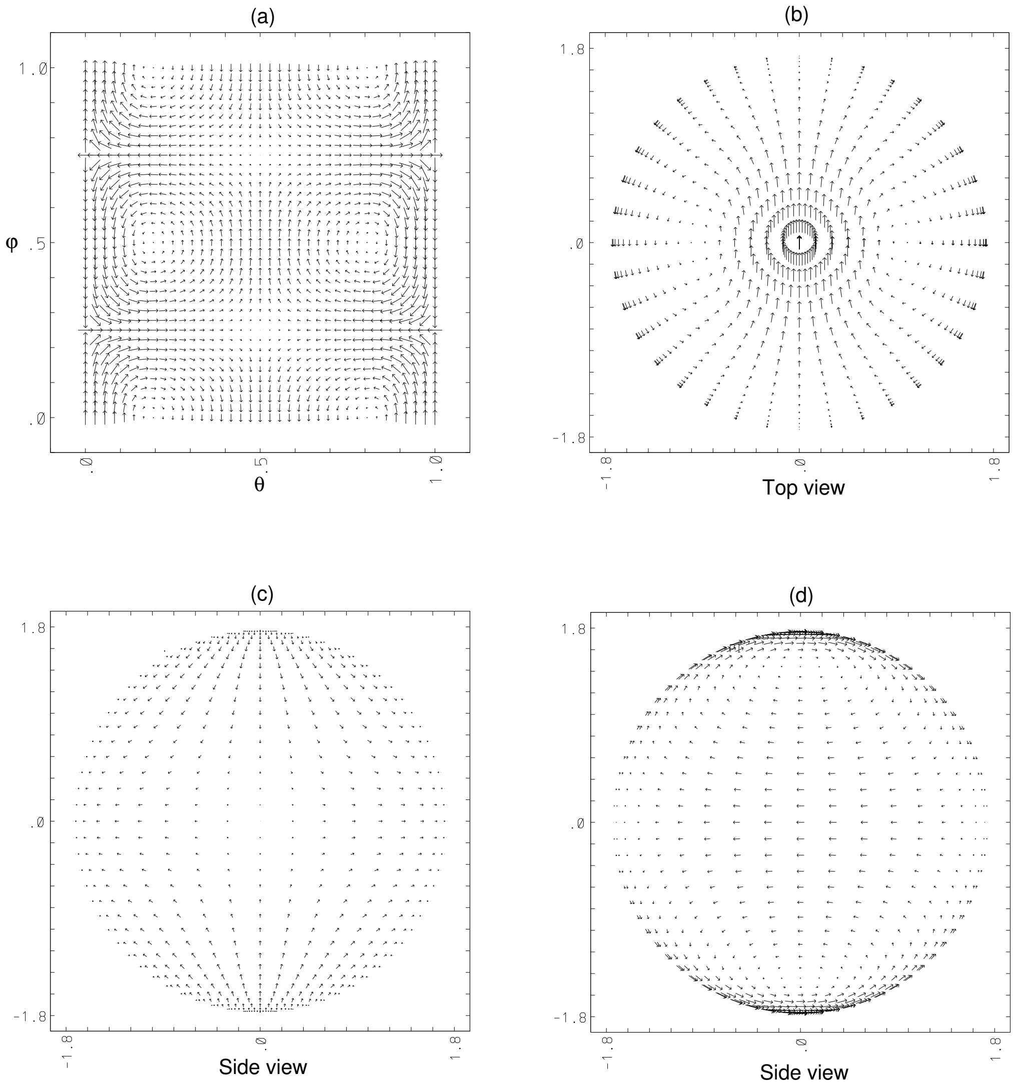

Figure 3: The induced current generated in a spherical shell by the shifting mode in a spheromak plasma. a) The projection in the ϕ–θ plane . b) Top view. Note the “figure-8” pattern centered at the poles of the shell. c, d) Orthogonal side views from the equatorial plane.

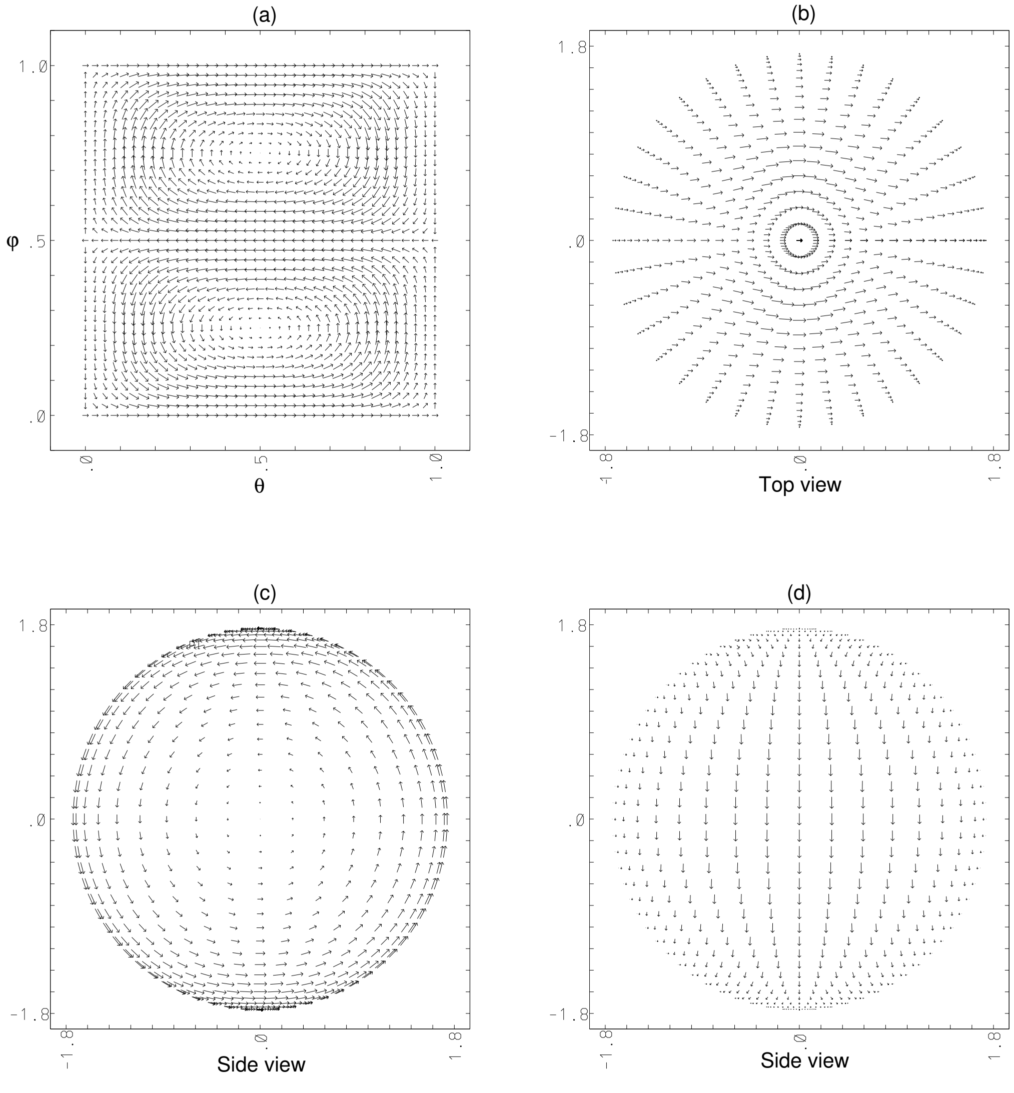

Figure 4: The eddy current generated in the conducting shell by the tilting mode. The projections are the same as for those in Fig. 3.

$$
\begin{aligned}
Q_Z &= \frac{Z_\theta}{X_\theta^2 + Z_\theta^2} \frac{\partial \chi_c}{\partial \theta}, \qquad (193) \\
Q_\phi &= \frac{1}{X} \frac{\partial \chi_c}{\partial \phi}.
\end{aligned}
$$

XIII. Magnetic perturbations at the Mirnov loops

Simulating the Mirnov loop measurements entails finding the magnetic perturbations throughout the vacuum region. In the previous sections the scalar potential on the surfaces have been calculated as a response to the plasma surface perturbation. This is extended into the vacuum region by a second application of Green's second identity for the observer points in the vacuum region and the source points on the surfaces:

$$
4\pi\bar{\chi}(\mathbf{r}) = -\int_S \bar{\chi}(\mathbf{r}')\nabla G(\mathbf{r},\mathbf{r}')\cdot d\mathbf{S}' + \int_{S_p} G(\mathbf{r},\mathbf{r}')\nabla\bar{\chi}(\mathbf{r}')\cdot d\mathbf{S}', \qquad (194)
$$

or, after the ϕ integrations,

$$
2\chi(\boldsymbol{\rho}) = -\int_C \chi(\theta')\mathcal{K}(\boldsymbol{\rho},\theta')\,d\theta' + \int_{C_p} \mathcal{G}(\boldsymbol{\rho},\theta')\mathcal{B}(\theta')\,d\theta', \qquad (195)
$$

where $\boldsymbol{\rho}$ is the positional vector in the (X, Z) plane and the trivial generalizations of the definitions in Eqs. (19) and (20) have been used. Note that the integrals here are singular if $\boldsymbol{\rho} \to C$; an efficient algorithm to accommodate this situation has not been implemented yet. In this limit, however, the perturbations can be calculated directly by Eq. (193).

One sees explicitly that the sources needed on the right hand side are the scalar potential, and its normal derivative on the plasma and conductor surfaces. As mentioned above, the former is already obtained as a response to the latter as described in the previous sections. The latter can also be obtained directly from the continuity of Q_n, the normal component of the perturbed field. The procedure is thus to carry out the calculations for δW_v, obtain the perturbations on the plasma surface from a suitable stability (eg. PEST) code, and also the response matrix for χ on the surfaces, and finally use Eq. (195) to determine $\chi(\boldsymbol{\rho})$. Hence, substituting for χ in terms of $\mathcal{B}$ from Eq. (107), Fourier analyzing, and using Eq. (119), one finds,

$$
\begin{aligned}
2\chi(\boldsymbol{\rho}) &= -i\sum_l (l - nq)\xi_l \left[\sum_k w_k \mathcal{C}_l(\theta'_k)\mathcal{K}(\boldsymbol{\rho},\theta'_k) - \sum_k^p \mathcal{G}(\boldsymbol{\rho},\theta'_k) e^{i[l\theta'_k - n\nu(\theta'_k)]} \right] \\
&\equiv -i\sum_l (l - nq)\mathcal{P}_l(\boldsymbol{\rho})\xi_l, \qquad (196)
\end{aligned}
$$

where

$$
\mathcal{P}_l(\boldsymbol{\rho}) = \sum_k w_k \mathcal{C}_l(\theta'_k)\mathcal{K}(\boldsymbol{\rho},\theta'_k) - \sum_k^p \mathcal{G}(\boldsymbol{\rho},\theta'_k) e^{i[l\theta'_k - n\nu(\theta'_k)]}. \qquad (197)
$$

The X and Z components of the magnetic field at the loops are found by calculating χ at four or more neighboring points around each loop position and then taking the appropriate spatial differences.

In the presence of a conducting shell, the normal component of the magnetic field calculated by this procedure correctly tends to zero as the observer point approaches the shell. The remaining component which lies within the plane of the shell is also seen to approach the value calculated

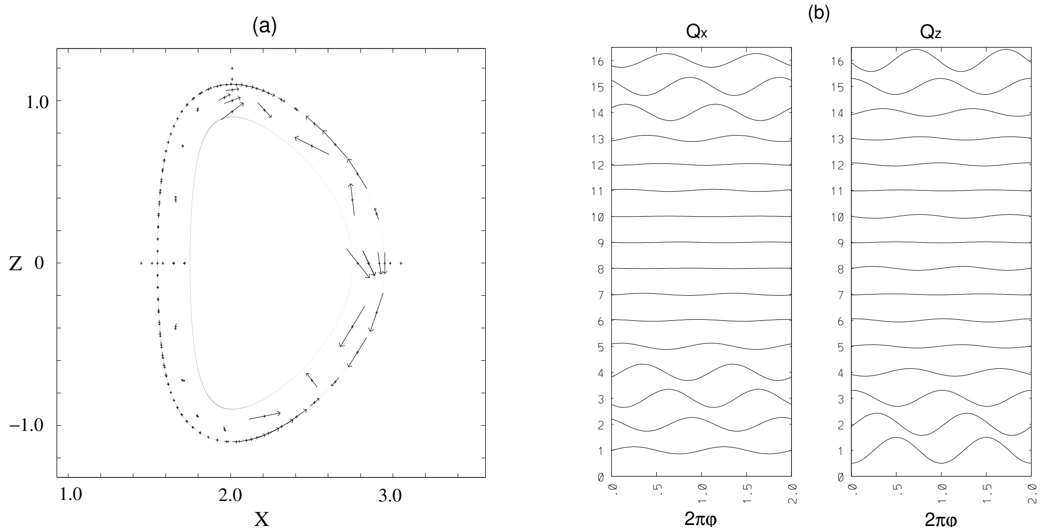

Figure 5: a) Magnetic perturbation vectors in the vacuum region and on the shell for the same case as in Fig. 2. The position of the loops are marked at the center of the arrows. Included are three sets which indicate the radial fall-off of the field. b) The variation of the perturbations, Q_X and Q_Z, as a function of ϕ simulates the toroidal rotation of the plasma.

directly by Eq. (193) in Sec. XII from χ on the surface. For a closed shell the field outside is also seen to vanish, typically to $\mathcal{O}(10^{-7})$ of the interior values. This is consistent with Eq. (195) and its analytic continuation on and beyond the shell. The algebraic fall-off of the field with minor radius, in the large aspect ratio circular case, has also been verified to have the behavior, $\delta B_{r,\theta} \sim r^{-l-1}$. These properties are illustrated in Fig. 5a by results from the same example of the kink unstable plasma of Sec. XII. Three sets of magnetic perturbation vectors are illustrated in the figure. A set of 16 loops are placed in the vacuum region between the plasma and the shell. Another set of 64 measurements are made directly on the shell. These latter points are located relative to the θ distribution of the grid points used in the plasma calculation in the PEST-1 code and thus are more sparsely spaced at the outer major radius side of the plasma. The third set of measurements are five observation points each at the inner and outer major radius sides and at the top of the plasma. These are distributed radially outwards to indicate the radial fall-off of the perturbation. The consistency between Fig. 2 and Fig. 5 is apparent.

In the experiments the signals on the Mirnov loops are detected because of the changing magnetic flux through the loops. If the mode is purely growing as is the case for an ideal MHD mode, the oscillatory part of this change usually arises through the plasma or mode rotation primarily in the ϕ direction so that the loops, in essence, measure the ϕ dependence of the modes. To simulate this rotation for comparisons with experimental results, the ϕ dependence is reinstated by appending the factor $\exp(-in\phi)$ into the expression for χ. Separation into real and imaginary parts gives

$$\begin{aligned}\bar{\chi}(\boldsymbol{\rho}) &= \frac{1}{2}\sum_l \xi_l(l-nq)\left[\mathcal{P}_l^R(\boldsymbol{\rho})\sin n\phi - \mathcal{P}_l^I(\boldsymbol{\rho})\cos n\phi\right. \\ &\quad \left. + \, i\left(\mathcal{P}_l^R(\boldsymbol{\rho})\cos n\phi + \mathcal{P}_l^I(\boldsymbol{\rho})\sin n\phi\right)\right]. \qquad (198)\end{aligned}$$

The X and Z components of the magnetic perturbation for each of the set of the 16 loop positions are displayed as a function of ϕ in Fig. 5b. Only two periods of rotation in ϕ are plotted so that the scale in time seems much more expanded than that usually seen in experimental data. As in the treatment of such data, the relative phases, magnitudes, etc. can also be simulated.

XIV. Usage and accuracy

The VACUUM code can be used as a stand alone unit by taking its input from files which controls the options and contain the data for the plasma parameters and, for the diagnostic runs, the surface MHD perturbations. VACUUM outputs the vacuum matrix appropriate for the various MHD stability codes. There are options for interfacing to the NOVA, ADJ, GATO, DCON, and the PEST codes. Alternatively, the VACUUM code can be hard-wired into these stability codes as is the case with the PEST system of codes.

The code is very robust in the sense that very little intervention is required for satisfactory accuracy. For almost all cases of interest, an accuracy to within 10^{-5} is easily achievable with a simple closed wall. For walls close to the plasma, the grid points of the wall and the plasma must be aligned properly as described in Sec. VII. For the segmented wall it's difficult to align the points, so that for accurate results the wall should not be placed too close to the plasma. A distance of about 5% should be acceptable. For similar reasons, the wall should not be too thin. Trial and error should determine the accuracy. An effective internal test for accuracy is the degree of symmetry of various matrices obtained in the calculation, including the output vacuum matrices. These symmetry tests are done routinely in the code. Calculations with the segmented shell have been benchmarked to ensure that the appropriate limits are approached in the limits of very large and very small gaps.

XV. Conclusions

A reliably accurate numerical procedure for solving Laplace's equation with Neumann boundary conditions in toroidally symmetric geometry with arbitrary plasma cross-sectional shape is described. The solution is cast as a response matrix to the plasma surface perturbation. The conducting material external to the plasma could be topologically spherical or toroidal – both enclosing the plasma, or toroidal but not enclosing the plasma. The spherical case is necessary for studying spheromak type plasmas or very small aspect ratio tokamaks, whereas the latter case realistically models shell configurations with toroidal gaps. One important result from using this option is a demonstration of the necessity for having the conducting shell localized at the major radius side of the plasma to help stabilize the external kink mode. In contrast to Fourier methods, the method of collocation used to solve for the surface scalar magnetic potential from the inhomogeneous Fredholm integral equation of the second kind which is generated from the use of Green's second identity is a most convenient and efficient way to treat these various conducting shell options. The vacuum energy is correspondingly expressed in terms of a plasma surface integral. The eddy currents and magnetic fields within the conducting shell proved to be useful diagnostic tools for understanding the magnetic perturbations in experiments as well as for designing feedback systems for tokamaks and spheromaks. The scalar potential away from the surfaces is also directly calculated by applying Green's second identity again but using the previously calculated surface fields as the new input boundary values. Together with the surface measurements this enables a direct comparison with the important experimentally observed Mirnov loop measurements. The driving source perturbation can, in general, be a set of source points, although conversion to a set of Fourier coefficients or finite elements makes more efficient use of computer memory. It is also shown how the magnetic vector potential can be calculated directly from the scalar potential. The code, VACUUM, has been interfaced quite successfully to a variety of MHD codes, and has the option to transform the vacuum energy matrix from the Fourier basis to a piecewise-constant finite element basis. Thus far, the code is applied to up-down symmetric configurations only, and the conducting shells are perfectly conducting. A non vertically symmetric version of the code is forthcoming. The generalization to resistive shells is more involved but is being formulated.

ACKNOWLEDGMENTS

This work is a result of the interaction over many years with many individuals, from the inception for fulfilling the needs of the PEST codes to the latest applications and interfacing with various other codes. The author gratefully acknowledges the important contributions from J.M. Greene, R. C. Grimm, J. L. Johnson, J. Manickam, N. Pomphrey, M. S. Chu, A. Turnbull, and J. S. Kim. Much of the inspiration for the development was motivated by fellow colleagues with their needs for applications to various devices. These invariably led to pleasurable and productive interactions with them – M. Okabayashi (PBX), S. Jardin (the Spheromak) and G. H. Neilson (TPX). Special thanks is also offered to J. M. Greene for his suggestions for improving the manuscript.

References

[1] R. C. Grimm, J. M. Greene, and J. L. Johnson, in *Methods in Computational Physics*, edited by J. Killeen, Academic Press, New York, 1976, volume 16 of *Controlled Fusion*, pp. 253–280.

[2] R. C. Grimm, R. L. Dewar, and J. Manickam, Journal of Computational Physics **49**, 94 (1983).

[3] C. Z. Cheng and M. S. Chance, Journal of Computational Physics **71**, 124 (1987).

[4] L. Bernard, F. Helton, and R. Moore, Computer Phys. Comm. **24**, 377 (1981).

[5] A. Glasser, The direct criterion of newcomb for the stability of an axisymmetric toroidal plasma, Technical Report LA-UR-95-528, Los Alamos National Laboratory, Los Alamos National Laboratory, Los Alamos, NM, 1995, Submitted to The Physics of Plasmas.

[6] S. C. Jardin, M. S. Chance, R. L. Dewar, et al., Nucl. Fusion **21**, 1203 (1981).

[7] I. B. Bernstein, E. A. Frieman, M. Kruskal, and R. M. Kulsrud, Proceedings of the Royal Society **244**, 17 (1958).

[8] B. M. Marder, Phys. Fluids **17**, 634 (1974).

[9] G. Dahlquist and Å. Björck, *Numerical Methods*, chapter 8, pp. 393,397, Prentice-Hall, inc., Englewood Cliffs, New Jersey, first edition, 1974.

[10] M. S. Chance, R. L. . Dewar, A. M. M. Todd, J. Manickam, R. C. Grimm, J. M. Greene, and J. L. Johnson, Comparison of different methods of calculating the vacuum energy in the PEST program, paper pc-5, in *Proceedings of the Eighth Conference on Numerical Simulation of Plasmas, Monterey, California*, number 8, Division of Magnetic Fusion Energy, Division of Laser Fusion, U. S. Department of Energy, 1978.

[11] R. Gruber, F. Troyon, D. Berger, et al., Computer Phys. Comm. **21**, 323 (1981).

[12] R. Gruber, S. Semenzato, F. Troyon, et al., Computer Phys. Comm. **24**, 363 (1981).

[13] R. Lüst and E. Martensen, Zeitschrift für Naturforschung **15a**, 706 (1960).

[14] M. S. Chance, J. L. Johnson, and R. M. Kulsrud, Plasma Phys. Controlled Fusion **36**, 1233 (1994).

[15] A. Erdélyi, *Higher Transcendental Functions*, volume 1 of *The Bateman Manuscript Project*, chapter 3, McGraw-Hill Book Co., Inc., New York, N.Y, Toronto, Canada, London, England, 1953.

[16] M. Abramovitz and I. A. Stegun, *Handbook of Mathematical Functions*, Number 55 in Applied Mathematics Series, National Bureau of Standards, Superintendent of Documents, U.S. Goverment Printing Office, Washington, D.C. 20402, ninth edition, 1970.

[17] F. Troyon, L. C. Bernard, and R. Gruber, Computer Phys. Comm. **19**, 161 (1980).

[18] G. Dahlquist and Å. Björck, *Numerical Methods*, chapter 7, pp. 297–301, Prentice-Hall, inc., Englewood Cliffs, New Jersey, first edition, 1974.

[19] H. Kugel, R. Bell, S. Bernabei, T. Chu, et al., Performance of the PBX-M passive plate stabilization system, in 15^{th} *IEEE/NPSS Symposium on Fusion Engineering*, volume 2, pp. 850–854, Piscataway, NJ 08854-4150, 1993, IEEE, The Institute of Electrical and Electronics Engineers.

[20] M. S. Chance, Y.-C. Sun, S. C. Jardin, C. E. Kessel, and M. Okabayashi, MHD stability of tokamak plasmas, in *Proceedings of the 2nd Symposium on Plasma Dynamics: Theory and Applications, University of Trieste, Italy (July 8-10, 1992)*, edited by M. Tessarotto, pp. 15–25, Trieste, Italy, 1992, Consorzio di Magnetofluidodinamica, University of Trieste.

[21] T. Ivers, E. Eisner, A. Garofalo, R. Kombargi, M. Mauel, D. Maurer, D. Nadle, G. Navratil, M. Sankar, M. Su, E. Taylor, Q. Xiao, R. Bartsch, W. Reass, and G. Wurden, Phys. Plasmas **3**, 1926 (1996).

[22]M. S. Chance, J. Bialek, S. C. Jardin, C. Kessel, J. Manickam, G. H. Neilson, and M. Okabayashi, Kink stability in tokamaks: Observation and suppression, in *Tokamak Concept Improvement*, edited by S. Bernabei, N. Sauthoff, and E. Sindoni, pp. 81–93, Via Castiglione, 101 - 40136 BOLOGNA - Italy, 1994, International School of Plasma Physics, Piero Caldirola, Società Italiana di Fisica.

[23]S. C. Jardin and U. Christensen, Nucl. Fusion **21**, 1665 (1981).

Appendix A. The vector potential

It is convenient to know both χ and $\mathbf{A}$. For example, calculations of the magnetic flux would involve more tractable line integrals of $\mathbf{A}$ rather than surface integrals of the magnetic field computed from $\nabla\chi$. The solutions for χ and $\mathbf{A}$ can be derived from each other as follows. Using

$$\mathbf{Q}_v = \nabla\chi = \nabla\times\mathbf{A}, \tag{A1}$$

we can solve for A_X and A_Z, assuming that A_ϕ is arbitrary for now, to obtain,

$$\begin{aligned} A_X &= -i\frac{X}{n}\left[\frac{\partial\chi}{\partial Z} - \frac{1}{X}\frac{\partial}{\partial X}XA_\phi\right], && \text{(A2)}\\ A_Z &= i\frac{X}{n}\left[\frac{\partial\chi}{\partial X} + \frac{\partial A_\phi}{\partial Z}\right], && \text{(A3)}\\ \text{and}\quad A_\phi &= A_\phi, && \text{(A4)} \end{aligned}$$

where it is assumed that perturbed quantities have the form $\sim\exp(-in\phi)$, with the restriction that $n\neq 0$.

Since $\mathbf{Q}_v$ is invariant under the gauge transformation:

$$\tilde{\mathbf{A}} \rightarrow \mathbf{A} + \nabla\Lambda, \tag{A5}$$

where Λ can be arbitrary, we choose

$$\Lambda = -\frac{i}{n}XA_\phi, \tag{A6}$$

so that, with

$$\nabla\Lambda = -\frac{i}{n}\left[\hat{\mathbf{e}}_X\frac{\partial}{\partial X}XA_\phi + \hat{\mathbf{e}}_Z\frac{\partial}{\partial Z}XA_\phi\right] - A_\phi\,\hat{\mathbf{e}}_\phi. \tag{A7}$$

we find

$$\begin{aligned} \tilde{A}_X &= -i\frac{X}{n}\frac{\partial\chi}{\partial Z}, && \text{(A8)}\\ \tilde{A}_Z &= i\frac{X}{n}\frac{\partial\chi}{\partial X}, && \text{(A9)}\\ \tilde{A}_\phi &= 0, && \text{(A10)} \end{aligned}$$

thus eliminating A_ϕ. Note that for calculating physical quantities like, e.g., the flux through a closed loop, there is no contribution from Λ since

$$\oint\nabla\Lambda\cdot d\mathbf{l} = \oint d\Lambda = 0. \tag{A11}$$

Conversely, one can use the ϕ component of Eq. (A1) to obtain χ from $\mathbf{A}$:

$$\chi = i\frac{X}{n}\left[\frac{\partial A_X}{\partial Z} - \frac{\partial A_Z}{\partial X}\right] = i\frac{X}{n}Q_{v\,\phi}. \tag{A12}$$